UNDERSTANDING AND CONTROLLING THE OPTOELECTRONIC PROPERTIES OF HYBRID PEROVSKITES FOR PHOTOVOLTAICS

Charles H. Van Brackle

A thesis submitted to the faculty at the University of North Carolina at Chapel Hill in partial fulfillment of the requirements for the degree of Master of Science in the Department of Applied Physical Sciences in the School of Arts and Sciences.

Chapel Hill
2020

Approved by:

Joanna M. Atkin

James F. Cahoon

Jinsong Huang

Scott C. Warren

Wei You

ABSTRACT

Charles H. Van Brackle: Understanding and Controlling the Optoelectronic Properties of Hybrid Perovskites for Photovoltaics
(Under the direction of Jinsong Huang)

Organic-inorganic hybrid perovskites (OIHP) have arisen in the past decade as a highly promising high-efficiency, low-cost technology for many semiconductor applications such as light emitting diodes (LEDs), radiation detection, and particularly photovoltaics. Relatively cheap materials and solution processability suggest low costs for perovskite solar cells (PSCs), but limits on efficiency and particularly stability ultimately limit their commercialization. To realize the full potential of PSCs, greater understanding and control of their optoelectronic properties and the tools used to probe them is needed. Here, a model of charge carrier dynamics demonstrates the effects of charge carrier trapping seen in time-resolved photoluminescence (TRPL) measurements, allowing for more accurate interpretation of the resultant decay lifetimes used to assess compositions or passivating agents. The efficiency of large-area PSC modules is increased through the development of large-area polymer scattering layers with improved light management that reduce reflective losses and increase photon absorption.

ACKNOWLEDGEMENTS

I would like to express my gratitude to my advisor Dr. Jinsong for his guidance and investment in my development both professionally and as a scientist. I would also like to thank the rest of my committee, including Dr. Joanna Atkin, Dr. James Cahoon, Dr. Scott Warren, and Dr. Wei You, for their scientific direction and advice in developing my thesis.

I would like to acknowledge the funding that supported this work from the National Science Foundation (Award DMR-1801741) and the Department of Energy/National Nuclear Security Administration (Award DE-NA0003921).

I would also like to acknowledge the members of the Huang group for their assistance running experiments and developing ideas that made this work possible. I would like to specifically thank Xuezeng Dai, Dr. Yehao Deng, Yuanxiang (Teddy) Feng, and Peter Rudd for their help as both fellow scientists and friends that supported me throughout my work.

Finally, I would like to thank my wife Sarah for providing me with unwavering support throughout my years of study and the courage to finish. This accomplishment would not have been possible without her.

TABLE OF CONTENTS

LIST OF FIGURES

LIST OF ABBREVIATIONS

AR	anti-reflection
BCP	bathocuproine
CdTe	cadmium telluride
CIGS	copper indium gallium selenide
C_{60}	fullerene
DMF	Dimethylformamide
EQE	external quantum efficiency
ETM	electron transport material
GaAs	gallium arsenide
HTM	hole transport material
IPCE	incident photon to current efficiency
ITO	indium tin oxide
J_{SC}	short circuit current density
LED	light emitting diode
MA(I)	methylammonium (iodide)
$MAPbI_3$	methylammonium lead triiodide
MHP	metal halide perovskite
OIHP	organic-inorganic hybrid perovskite
OPV	organic photovoltaic
PCE	power conversion efficiency
PDMS	polydimethylsiloxane
PL	photoluminescence

PSC	perovskite solar cell
SQ	Shockley-Queisser
TCO	transparent conducting oxide
TCSPC	time-correlated single photon counting
TRES	time-resolved emission spectroscopy
TRPL	time-resolved photoluminescence
V_{OC}	open circuit voltage

CHAPTER 1: INTRODUCTION TO CHARGE CARRIER GENERATION AND RECOMBINATION IN HYBRID PEROVSKITES

1.1 Introduction to Perovskite Solar Cells

Organic-inorganic hybrid perovskites (OIHP) are the newest class of thin-film photovoltaics to show great promise towards the development of a low cost, abundant form of renewable energy. These hybrid materials, which crystallize in the characteristic calcium titanium oxide

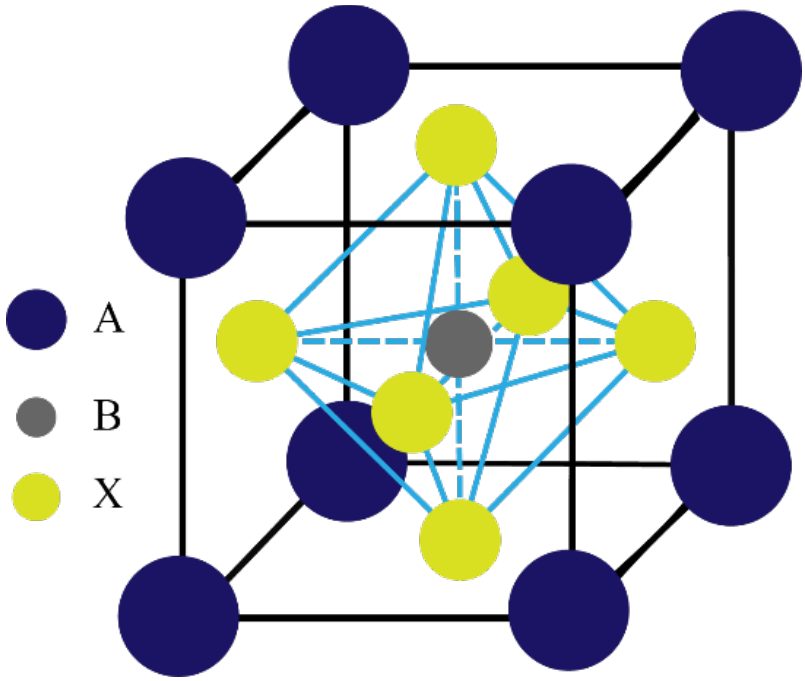

Figure 1.1 ABX_3 perovskite structure.

A = organic/inorganic monovalent cation

B = inorganic metal divalent cation

X = halide anion

perovskite structure of ABX_3 (Fig. 1.1)—where A is a monovalent organic or inorganic cation (e.g. methylammonium, formamidinium, Cs, or Rb) B is a divalent metal cation (e.g. Pb or Sn), and X is a halide anion (I, Br, or Cl)—form semiconductors with a wide range of applications. Since their first use in photovoltaic cells as visible-light sensitizers just over a decade ago[1], halide perovskites have seen significant development in the areas of photovoltaics, light emitting diodes (LED)[2], radiation detection[3,4], neuromorphic computing[5], and more. Power conversion

efficiencies (PCE) of perovskite solar cells (PSC) have already eclipsed 25%[6], exceeding existing thin-film photovoltaic technologies such as cadmium telluride (CdTe)[7] at 22.1% and copper indium gallium selenide (CIGS) solar cells[8] at 23.4%.

The soaring efficiencies of PSCs in recent years are certainly impressive; however, it is the versatility of hybrid perovskites that grants them so much potential. Many permutations of compositions based on the ABX_3 structure give hybrid perovskites a tunability that yields a wide range of applications; modifying the bandgap with different cations and anions opens up the possibility of perovskite-perovskite and perovskite-silicon tandem architectures for solar cells[9–12]. Excellent solubility of many of the common OIHP materials allows for films or crystals to be processed by solution, meaning low temperature, scalable manufacturing processes are possible and already being realized[13–17]. This and the relative abundance of the materials suggests low cost, large scale production of perovskites devices is feasible.

In addition to bandgap tunability and solution processability, the great promise of perovskite photovoltaics is attributed to strong absorption in the visible range with a sharp absorption edge[18,19], low exciton binding energies[20–22], long carrier diffusion lengths and lifetimes[23–28], and defect tolerance[29]. However, many challenges remain to see their implementation as a commercial solar solution. Thermal, moisture, UV-irradiation, light degradation pathways lie among others as sources of instability in thin-film OIHP photovoltaics[30]; a significant efficiency gap between the highest device efficiencies and the Shockley-Queisser (SQ) Limit—the maximum theoretical PCE of a single junction solar cell—remains[31]. Despite their impressive efficiency gains in recent years, PSCs still remain well below the approximately 33% limit imposed by radiative recombination between holes and electrons. If perovskites are to usurp existing photovoltaic technologies, this 8% efficiency gap must be closed by designing

compositions, fabrication techniques, and passivating agents that limit material defects, which serve as sites where photoexcited charges can be trapped and recombine nonradiatively, contributing nothing to device performance and increasing thermal degradation. Careful control of a perovskite's charge recombination processes will yield more efficient use of all absorbed photons, and thus a more efficient solar cell.

1.2 Photogenerated Excitons and Free Charge Carriers

An important question for any semiconductor acting as a light-harvesting material in a photovoltaic device stack is whether photoexcitation produces dominant excitonic or free charge carrier characteristics[20]. If a photon excites an electron and a hole, Coulombic forces can lock this charge pair—an exciton—into a bound state that cannot contribute to the photocurrent of the device. If the binding energy barrier is low enough, thermal energy is sufficient to dissociate the exciton for collection by the electron and hole transport materials (ETM and HTM). Inorganic materials in photovoltaics such as silicon and gallium arsenide (GaAs) have been shown to have exciton binding energies below $k_B T$ at room temperature (~ 26 meV)[32,33]. This is in contrast with organic photovoltaics (OPV), which have materials with exciton binding energies on the order of hundreds of meV; this is a significant limiting factor to current generation and to the open-circuit voltage V_{oc} for these solar cells[34,35]. Thus, donor/acceptor bulk heterojunctions (e.g. P3HT and PCBM bulk heterojunction solar cell) are necessary to dissociate excitons for charge collection in OPVs.

Halide perovskites have been studied extensively to discover the nature of the photogenerated charges found in these organic-inorganic hybrid materials. Savenije et al. used temperature-dependent steady-state photoluminescence (PL) measurements to estimate the exciton binding energy E_b in $(CH_3NH_3)PbI_3$ (i.e. $MAPbI_3$)[36]. Observing a decrease in PL

intensity with increasing temperature, there was strong indication of thermal activation and they fit the luminescence data with the Arrhenius equation:

$$I(T) = \frac{I_0}{1 + Ae^{(-E_b/k_BT)}} \qquad \textbf{(1)}$$

yielding an exciton binding energy of 32 ± 5 meV. Sun et al. also made use of this temperature-dependent PL technique to estimate an exciton binding energy of 19 ± 3 meV for $MAPbI_3$ in their perovskite-fullerene bilayer[37].

Hu et al. reported distinct excitonic and free charge carrier behavior in methylammonium lead trihalides using several methods for confirmation[38]. Using impedance spectroscopy, the authors measured the dielectric constant in $MAPbI_3$, finding a large value over a wide-range of frequencies. In organic semiconductors, it is known that the large exciton binding energies of 0.3-1.2 meV are a result of low dielectric constants that do not effectively screen the Coulomb interactions between the paired charges[39]. A large relative dielectric constant around 32 for $MAPbI_3$ at high frequencies is sufficient to screen the Coulomb forces necessary for an excitonic material (ref 38). The authors calculated the excitonic binding energies of $MAPbBr_3$ and $MAPbBr_{3-x}Cl_x$ from the full-width half maxima of the observed strong excitonic peaks found in the absorption spectra. These larger bandgap perovskites (relative to $MAPbI_3$) with Br and Cl were found to have larger excitonic binding energies of 80 and 87 meV, respectively. Finally, the authors showed the field independence of exciton dissociation in $MAPbBr_3$/fullerene bilayers. Incident photon to charge carrier efficiency (IPCE) was used to measure external quantum efficiency (EQE) of a perovskite/fullerene (PCBM or ICTA) device. They observed an EQE increase in the absorption range for the fullerenes (560-750 nm) as the bias was varied from 0 to 0.8×10^5 V cm^{-1}; however, the EQE change over the perovskite absorption band was negligible, suggesting that all excitons were already dissociated in the $MAPbBr_3$ with or without the applied

electric field. The work by Hu et al. demonstrated several techniques to observe clear non-excitonic behavior in methylammonium lead trihalide perovskites and found higher excitonic binding energies > 80 meV in higher bandgap metal halide using Br.

It is clear that for hybrid perovskites there is a relatively wide range of reported exciton binding energies, even for a single material such as $MAPbI_3$. If we look even further to 2D layered perovskites, we find that their exciton binding energy values are typically one order of magnitude higher (> 200 meV)—due to quantum confinement—than those observed for the 3D perovskites used for the most efficient PSCs. Nonetheless, it is also clear that these estimates of E_b are quite dependent on other factors such as dielectric constant and temperature. More importantly, there is no doubt that the exciton binding energies for these materials are comparable to inorganic semiconductors such as GaAs[33] and thus comparable to the thermal energy at operating conditions for PSCs. These low exciton binding energies mean that charges are easily dissociated into free charge carriers which contribute to the high performance of OIHP in photovoltaic applications.

1.3 Charge Carrier Recombination

For photovoltaic applications, long charge carrier lifetimes are important to ensure charges are completely extracted by the transport materials to the electrodes and to produce high open-circuit voltages. The absence of trapped charges and short recombination lifetimes raises the steady-state charge carrier density under irradiation, thereby increasing the quasi-Fermi level splitting and the resultant open-circuit voltage of the device. However, if charges recombine before they are extracted, this can be detrimental to internal quantum efficiency of a device. There are several mechanisms of recombination in OIHP, and the dynamics of the processes are described by the rate equation:

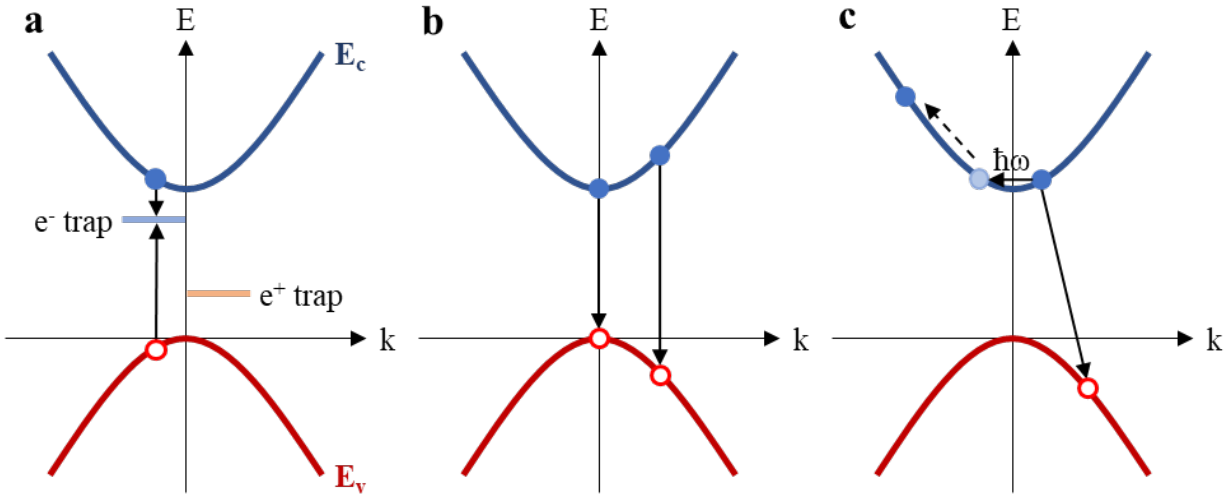

Figure 1.2 Recombination mechanisms in hybrid perovskites. **(a)** Trap-assisted recombination, also called monomolecular or Shockley-Read-Hall recombination, occurs when the recombination is facilitated by an electron's (or conversely a hole) capture by a trap state—typically a defect state. **(b)** Bimolecular recombination is the recombination of an electron in the conduction band with a hole from the valence band. **(c)** Auger recombination includes several charges, where an electron and hole recombine along with and energy/momentum transfer to a third electron or hole (here, a phonon is transferred to a second electron).

$$\frac{dn}{dt} = G - k_1 n - k_2 n^2 - k_3 n^3 \quad \textbf{(2)}$$

where G is the rate of charge generation, $k_1$is the monomolecular recombination rate, $k_2$is the bimolecular recombination rate, and $k_3$is the Auger recombination rate[40]. At solar cell operating conditions under standard AM 1.5 light of 100 mW cm^{-2}, initial carrier densities are approximately 10^{16}-10^{17} cm^{-3} and bimolecular recombination is the dominant recombination mechanism[26], though the trap-assisted mechanism can still be very much relevant. The bimolecular recombination pathway (Fig. 1.2b) is the recombination of an electron and a hole—the inverse of absorption[41]. At lower excitation densities, the trap-mediated monomolecular recombination (Fig. 1.2a) is most significant; defect states in the bandgap can capture electrons or holes, which are either emitted to the carrier bands by phonon absorption or recombine from

the trapping state[42]. Auger recombination (Fig. 1.2c) is a multi-charge non-radiative process whereby an electron and hole recombine, and energy and momentum are transfer to a third electron or hole. This mechanism is strongly dependent of charge carrier density and its non-radiative nature limits the ideal performance of a material; fortunately, Auger recombination is very weak at operation conditions in PSCs[43].

Monomolecular Recombination

The first order mode of charge-carrier recombination in semiconductors is a process involving a single charge carrier; an electron or a hole (or an exciton in the case of an excitonic material) can become trapped or captured by a sub-bandgap state—a defect state. The trapped charge can be reemitted into its respective band by phonon interaction if the trap is shallow and thermal energy is sufficient for reemission; however, if the trap is a deep energy trap, then the time for emission will be very large and the charge will likely recombine with an opposite charge before emission. Monomolecular recombination, also known as Shockley-Read-Hall (SRH) recombination—the rate of this process is governed by SRH statistics—is typically a non-radiative recombination process and point of loss in solar cells[42,44]. Though hybrid perovskites are a relatively defect tolerant material[29], it is clear that trap-assisted recombination will be heavily influenced by trap density, depth, and type—and thus also greatly influenced by the processing conditions which bring about the defect states. Because of weak levels of Auger recombination in PSCs (see 1.3.3 Auger Recombination), defect-mediated recombination is perhaps the largest source of loss plaguing hybrid perovskites[43]; therefore, numerous studies have been undertaken to quantify and suppress monomolecular recombination, using techniques such as and terahertz transient absorption[24,45], photoconductivity[46,47], or time-resolved photoluminescence[26,28,48].

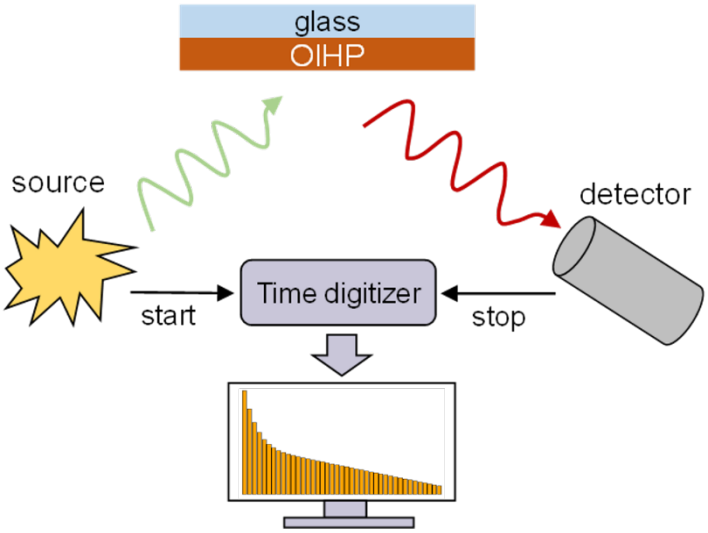

Figure 1.3 Measuring fluorescence lifetime with TCSPC. A pulsed excitation source (e.g. pulsed diode laser) excites an OIHP thin film. The time digitizer starts the clock at start signal from the excitation pulse and receives a stop signal from the detector as it observes a single photon from the fluorescence of the film. The start-stop time is recorded, and a histogram is quickly recorded as the repetition rate of the start-stop sequence is typically 100 kHz-100 MHz for OIHP used for photovoltaics. The resultant histogram represents the photoluminescence response over the time after excitation.

One of the most common methods to these processes such as SRH recombination is by using time-correlated single photon counting (TCSPC) to measure TRPL. TCSPC (described in Figure 1.3) is a simple but powerful way to measure the lifetime of the photoluminescence response of a material, and is a quick indicator of the quality of a material after some change to fabrication process, doping, passivation, or other effects. For hybrid perovskites and other semiconducting materials, it is typical to determine the change in quality—long charge carrier lifetimes are good as they ensure charges are better separated to their respective transport layers—as a longer TRPL lifetime generally indicates longer charge carrier lifetime (see Chapter 2).

Solution-processability is perhaps the most advantageous feature of hybrid perovskites, because of the possibilities offered in the way of low-cost, scalable semiconducting materials for a wide-range of applications. However, processing conditions often bring about different defect states which act as SRH recombination centers[49]. Using both steady-state photoluminescence and TRPL, deQuilettes et al. observed bright and dark regions which they postulate were due to defect states—in $MAPbI_3(Cl)$ thin films[26]. The authors show fluence-dependent PL transients for

the bright (high PL emission) and dark (low PL emission) regions, noting how the PL decay for the dark region requires higher excitation fluences to express bimolecular-dominate recombination; in addition, they claim that the 1st order PL decay lifetimes are shortest in the grain boundaries, compared to the bright and dark regions. Stranks et al. also demonstrates this transition of PL transients from monomolecular to bimolecular as excitation intensity is increased[48]. The authors observe how the steady-state PL intensity increases after the first few seconds after illumination begins (on the order of seconds); from these observations, the authors assert that as traps are filled—by either higher fluence in transients or prolonged exposure in steady-state—radiative (i.e. bimolecular) recombination strengthens. They also demonstrate device V_{OC} increasing similarly over the same time frame as the steady-state PL, linking the device performance to increased radiative recombination.

The observation of decreased lifetimes at grain boundaries (GB) by deQuilettes et al. implies that GBs could be a primary source of non-radiative recombination in OIHP. Other works assert the non-radiative recombination in perovskite thin films is dominated by GBs, as larger grain sizes often lead to improved device performance[50]. Xiao et al. demonstrate increased charge mobility and device performance from larger grains produced by solvent annealing[51]. Works using passivating molecules (such as pyridine) largely attribute improved transient PL lifetimes and reduced non-radiative recombination to passivating defects (e.g. undercoordinated Pb atoms) in the grain boundaries, suggesting the GBs are not benign to charge carriers[26,52,53]. However, attributing the significantly improved device performance to passivating GB defects runs counter to the idea that polycrystalline hybrid perovskites are largely defect tolerant, due to low amounts of deep traps[29,54,55]. Using time-resolved microwave conductivity (TRMC), Reid et al. observe both decreased charge mobility in the presence of *decreased* grain size and decreased

carrier lifetime in the presence of *increased* grain size[56]. The former agrees with the studies showing larger grains equals improved device performance; however, the latter predicts slower recombination for the smaller grains, which have a greater GB surface area. Yang et al., through the use of high-resolution confocal fluorescence lifetime imaging (FLIM), presented highly uniform grains with respect to PL intensity and lifetime; they observed statistically that with increased grain area, average lifetime of a grain increased, while average PL intensity decreased. The high-resolution FLIM technique allowed the authors to resolve the PL intensity and lifetime measurements along line scans across grain boundaries. They saw that though PL intensity decreased in the grain boundary, PL lifetime would actually increase or equal the value of the adjacent grains' interior. Though the use of confocal FLIM is strictly a surface technique, the authors demonstrate GBs are not necessarily the dominant recombination centers relative to grain interiors they were previously thought to be; however, the decreased luminescence at the GBs does indicate that specifically non-radiative, monomolecular recombination may be higher at the GBs. The work by Yang et al. suggests that though they limit charge carrier diffusion, grain boundaries may be relatively benign with respect to recombination in hybrid perovskites[55,57].

The measurement of TRPL as recorded by time-correlated single photon counting (TCSPC) as a method of measuring recombination lifetimes is commonplace throughout many studies. However, often the lifetimes of PL transients are extracted from the TRPL measurements and taken directly to be the monomolecular (or sometimes bimolecular) recombination lifetime. This may not always be the accurate (see Chapter 2); frequently there is a biexponential decay with a fast and slow component to the PL transients[58], where each component lifetime could be comprised of both trapping and radiative recombination. Maiberg et al. modeled time-resolved luminescence in semiconductors, focusing on the sub-band gap

trapping states responsible for Shockley-Read-Hall recombination[59]. Their model simulates both monoexponential and biexponential transients, and the model attributes the initial, fast decay to charge capture and recombination, while the second slow, decay is defined by trap emission, re-capture, and recombination. Temperature dependent simulations show that increased temperature can reduce the necessary excitation fluence required to reduce carrier trapping. This work, which is generalized to any semiconductor, provides a model to better dissect TRPL transients to reveal valuable information about the recombination mechanisms of the material, which can be otherwise muddled by a blend of monomolecular and bimolecular recombination at excitation fluences below or comparable to 1 sun intensity.

Recent work in hybrid perovskites has frequently focused on examining the properties of mixed-cation (such as Cs or Rb incorporation) or methylammonium-free perovskites to improve stability or performance[60–63]. Different perovskite compositions are sure to have varied film morphologies and trap densities, and thus widely varying recombination kinetics. Recently, Solanki et al. demonstrated that incorporation of Rb^+ ions accompanied by Cs^+ ions (without Cs, the authors saw poor integration of Rb with MA and FA) produced a quaternary-cation perovskite with increased grain size, carrier lifetime, and PCE[64]. They assign the decreased monomolecular recombination rate—estimated from TRPL—in the RbCsMAFA perovskite to reducing the trap density—relative to the MAFA perovskite—from 7.4×10^{17} cm^{-3} to 3.5×10^{17} cm^{-3}. From this and PLQE measurements, the authors assert that Rb and Cs incorporation into MAFA perovskite essentially passivate bulk defects and suppress surface recombination. It is possible that the mixed-cation perovskites have reduced strain within the perovskite lattice by reducing the density of defect states, as strain has been shown to have detrimental effects to PSC operation[65]. Pairing scanning micro-x-ray diffraction (XRD) and

photoluminescent lifetime imaging, Jones et al. demonstrated that local strain due to defects (e.g. halide vacancies) was correlated with trap-assisted, non-radiative recombination[66]. Building on these works could show promising results in improving stability of PSCs through exploration of reduced monomolecular recombination due to reduced strain.

Bimolecular Recombination

As monomolecular recombination is suppressed—either by eliminating the defects which trap electrons and holes or by increasing excitation intensity—bimolecular recombination emerges as the dominate recombination mechanism in semiconductors. This process is intrinsically radiative and can be considered to be the inverse of the absorption process[41]; Davies et al. used the van Roosbroeck-Shockley relation[67] to extract bimolecular recombination rate constants from absorption spectra and compared them to k_2 estimated from transient THz photoconductivity spectra. Finding agreement in the rate constant estimates over wide-range of temperatures (50-300 K), the authors confirmed this inverse-relationship of absorption and bimolecular recombination. The bimolecular recombination rate constants shown by Davies et al. prove to be far lower than what is suggested by the Langevin model, which relates the bimolecular recombination rate constant to charge mobility in a semiconductor[68–70], given by

$$k_2 = \frac{e^{-}\left(\mu_e + \mu_p\right)}{\epsilon} \qquad (3)$$

where e^{-} is the electron charge, μ_e and μ_h are the electron and hole mobilities, and ϵ is the dielectric constant. Materials with recombination rates well below Langevin predictions are actually sought after, as they reduce open circuit voltage losses[71]; this has been demonstrated in perovskites—in one study, values of k_2 for both $MAPbI_3$ and $MAPbI_{3-x}Cl_x$ four orders of magnitude below the Langevin prediction were reported[24]—and other semiconductors known as excellent photovoltaic materials, such as GaAs[72]. Though radiative recombination is beneficial,

low bimolecular recombination rates with high charge mobilities (i.e. non-Langevin) mean that charges can diffuse further before recombining, increasing the likelihood of charge extraction in a device. Wehrenfennig et al. use transient absorption spectra to study the bimolecular recombination rates and charge mobilities in $MAPbI_{3-x}Cl_x$, demonstrating an estimation of k_2 that differs from the Langevin model (using the calculated carrier mobility) by approximately five orders of magnitude[73]; this non-Langevin limited yields a diffusion length L_D of around 3 μm, whereas a material that follows the model would only enjoy about 100 nm[22,73].

Although trap-mediated and Auger recombination are detrimental to device performance, bimolecular recombination is a radiative process, opening up the possibility for emitted photons from recombination to be reabsorbed as part of a photon recycling process. The photon recycling process can thus effectively increase the PLQE of a perovskite sample; combined with textured substrates reported by Richter et al that can substantially enhance light-out-coupling[74], or a polydimethylsiloxane (PDMS) anti-reflection layer for improved light management (see Chapter 3)[75], the external PLQE of hybrid perovskites can be significantly improved despite low internal PLQE relative to materials such as GaAs (over 99%)[76]. Braly et al. reported an internal quantum efficiency η_{int} of 91.9% in $MAPbI_3$ thin films under one sun illumination using *n*-trioctylphosphine oxide (TOPO) to bind to the film surface and reduce non-radiative recombination,[77] drawing comparisons to reports[52,78] of Lewis base passivation. However, further work will be needed to explore the mechanisms through which the improved transport length arises. Photon recycling has also been demonstrated in in single crystalline $MAPbI_3$ and $MAPbBr_3$ by Fang et al., who used polarization differences to distinguish filtered photons from reemitted photons from a reabsorption process[79]. However, the authors calculated a photon recycling efficiency of only about 0.5% for both perovskites, which is negligible under one sun

illumination; they posit this is due to low PL quantum yields in these materials. Careful methods to increase PLQE by ensuring bimolecular recombination is the dominant mechanism under solar operating conditions—whether that be through increased photon recycling or suppressed trap-assisted recombination—will bring PSCs closer to the radiative limit.

Auger Recombination

The Auger process of recombination in semiconductors is fundamentally non-radiative. An electron undergoes annihilation with a hole and the recombination energy is transferred to a third particle (Auger recombination can also occur between two excitons); thus, no photon is emitted[80,81]. As a result, and as shown by its third order dependence in Eq. 2, Auger recombination is strongly dependent on the charge carrier density. Fortunately for PSCs, Auger recombination is weak at carrier densities relevant for photovoltaic operations; this is in stark contrast with silicon, where strong Auger recombination is largely responsible for the large discrepancy between the SQ limit of 33% and the 1-sun efficiency limit of 29% for c-Si[43,82]. The V_{OC} loss in halide perovskite solar cells due to Auger recombination is less than 2 mV from the radiative limit[43], which is quite small relative to the losses contribute by SRH recombination and other sources.

Terahertz (THz) transient photoconductivity measurements has been used to measure the Auger and bimolecular rate constants for a formamidinium lead perovskite $FAPb(Br_yI_{1-y})_3$, where y changes to vary the Br/I ratio[83]. Both rate constants increase monotonically with increasing bromide content, and it was shown that pure Br at the X_3 site yields an Auger recombination rate one order of magnitude greater than the pure I metal halide. However, both rates were insensitive to the crystallinity, suggesting an inherent link with the rate constants and the electronic structure. Another study using THz spectroscopy by Milot et al. demonstrated a strong

relationship between k_3 and the phase of the perovskite, with different temperature dependent trends for each of the orthorhombic, tetragonal, and cubic phases. The authors assign this to strong influence the electronic band structure[84]—which can be significantly altered due to different degrees of hydrogen bonding and spin-orbit coupling[85]. These findings suggest that despite the fact that Auger recombination can become a major form of non-radiative loss in perovskites for high charge-carrier densities ($> 10^{18}$ cm^{-3}), proper electronic band structure manipulation could limit the Auger process. Shen et al. present a similar solution, wherein tuning the perovskite composition to minimize metal-halide lattice distortions should suppress Auger recombination[86]. Density functional theory (DFT) calculations showed that fixing the Pb and I atoms in the $MAPbI_3$ lattice yielded a reduced k_3 rate.

Though Auger recombination may often be negligible for solar cell applications, the phenomenon can become relevant in applications that require high charge-carrier densities, such as solar-concentrator uses or lasing[87]. Xing et al. demonstrated amplified spontaneous emission (ASE) in solution-processed $MAPbI_3$; they calculated a carrier density threshold of 1.7×10^{18} cm^{-3} required for ASE, which is typically the regime of densities relevant to Auger recombination. However, they report that their "bulk-like" $MAPbI_3$ film did not suffer much from Auger losses because of a relatively long Auger lifetime (τ_{Aug} ~ 300 ps). This study agrees with the implications of the work by Milot et al. above; despite a relatively high charge-carrier density, Auger recombination was not a major source of non-radiative losses. Defect physics—which influences the electronic structure of the perovskite—could indirectly affect the Auger process in their $MAPbI_3$.

Though monomolecular and bimolecular recombination are the dominant charge-carrier recombination mechanisms for photovoltaic applications, important work with hybrid

perovskites has shown that the Auger process cannot be completely disregarded, and certainly not for applications with which require high charge-carrier densities. To avoid the limitations of Auger losses seen in crystalline silicon[88], controlling band structure or distortions of the metal-halide octahedra will be necessary. This will go a long way in reaching the quantum efficiencies enjoyed by traditional III-V semiconductor devices, such as GaAs solar cells[86,89].

1.4 Conclusion

Organic-inorganic hybrid perovskites have been the topic of intense research in the photovoltaic community over the last decade due to their outstanding photonic and electronic properties. Much of this can be attributed to the favorable non-excitonic character of hybrid perovskites; reports of low excitonic binding energies and efficient charge dissociation were reviewed, showing a wide-range of estimates for E_b in $MAPbI_3$ due to its strong temperature and phase dependence. Additionally, losses due to Auger recombination are largely negligible at operating conditions relative to photovoltaic applications, though they can be significant for other higher charge carrier density applications such as lasing. However, nonradiative recombination mediated by defect states account for much of the losses in PSCs that hinder their PCE and thus ultimately their commercialization.

CHAPTER 2: OBSERVING CHARGE TRAPPING IN METAL HALIDE PEROVSKITES USING TIME-RESOLVED PHOTOLUMINESCENCE

2.1 Introduction

The rapid rise of metal halide perovskites (MHP) is frequently attributed in part to their relatively good defect tolerance[29]; however, perovskite solar cells remain hampered by high densities of defects, particularly at the film surface and grain boundaries, that serve as pathways for material degradation and nonradiative recombination[90]. Examination of their charge carrier recombination lifetimes is a common practice when judging a new composition, fabrication technique, or passivating agent and its effects on the nonradiative recombination mechanisms within a thin film. This first evaluation is often provided by studying a perovskite film's fluorescence lifetime.

Time-resolved photoluminescence is a commonly used method for fluorescence lifetime measurements and is frequently implemented to measure bulk time-resolved photoluminescence transients in hybrid perovskites[68,91] and other semiconductors[92–94]. The resulting TRPL decays are used to estimate charge recombination lifetimes, extracting the values from fits of charge carrier recombination models[48] or directly from the lifetime of the decays themselves. The passivating effects of many different molecular structures such as Lewis acids[95], Lewis bases[52,78], or dual charged zwitterions[96] are frequently corroborated by TRPL transients, made evident by their influence on the PL transients. Many measurements have been typically carried out with photogenerated carrier densities below those for photovoltaic operation, and often exhibit single exponential, biexponential, or stretched exponential decay processes whose presence and

characteristics depend strongly on the perovskite composition, fabrication method, and material quality. This complete context, if not given, can obscure the origin of the decay processes found in these biexponential transients, clouding the meaning of the resultant TRPL lifetimes. Several scenarios have been offered to explain the fast and slow components of the biexponential decays: surface and bulk recombination[97,98], charge carrier diffusion and radiative recombination[99], monomolecular (1st order) and bimolecular (2nd order) recombination[48], and charge trapping and detrapping[59,100]. Single photon and two-photon excitation have been used to probe the surface and bulk recombination kinetics of $MAPbI_3$ and $MAPbBr_3$ single crystals[97], respectively, showing faster lifetimes were associated with quick charge recombination at defective crystal surface for those unpassivated single crystals. For perovskite thin films used for photovoltaic and photodetector applications, film thicknesses are quite thin. For a MHP film with a modest carrier mobility of ~ 50 $cm^2\ V^{-1}\ s^{-1}$ (ref [68]) and 500 nm thickness, the carrier distribution in vertical direction would be nearly uniform in less than 300 ps. This redistribution of photoexcited carriers happens much quicker than most radiative recombination process in perovskites. Similarly, in the case of non-imaging type TRPL measurement (i.e. not a fluorescence lifetime imaging microscopy (FLIM) system), the excitation beam diameter is typically on the order of millimeter, far too large for lateral carrier diffusion to be at play in these measurements. The 2nd order bimolecular recombination process typically only arises or dominates when excitation levels have reached or exceeded 10^{16}-10^{17} cm^{-3} (it is very sample dependent), which is at or higher than one sun solar cell operating conditions.

Below these carrier concentration levels in low fluence TRPL measurements, the trap-mediated recombination processes in the metal halide perovskite films are explored. Here, using time-resolved fluorescence techniques, we probe the trapping and detrapping processes

responsible for the characteristic biexponential decays so commonly observed in the PL transients of MHP thin films. We observe the strong influence of charge carrier trapping on the TRPL curves, which is strongly dependent on film quality and experimental conditions. Films with higher trap densities can actually demonstrate longer TRPL lifetimes, suggesting that longer PL decay lifetimes do not necessarily equate to perovskite films with improved optoelectronic properties. We utilize a model of charge trapping, detrapping, and recombination to show the strong influence on the TRPL transients made by trap stat distributions and capture mechanisms, which in the presence of strong trapping manifest as strict biexponential decay transients.

2.2 Film Fabrication and Characterization

Unless stated otherwise, all materials and solvents were sourced from Sigma-Aldrich. Methylammonium iodide (MAI) was purchased from GreatCell Solar. Lead iodide (PbI_2, 99.999%) was purchased from Alfa Aesar. All materials were used as purchased.

Glass substrates (1.5 x 1.5 cm) were cleaned via iterative ultrasonication of soap, acetone, and isopropanol. Films were deposited by either spin or blade coating. For spin coating $MAPbI_3$, MAI and PbI_2 (1:1 ratio) were dissolved in *N,N*-dimethylformamide (DMF) to produce the 1.2 M perovskite precursor, which was filtered before use. The glass substrates were subjected to a 20 min UV-ozone treatment immediately prior to film fabrication; 80 µL of precursor ink was deposited onto the substrate and spun for 30 sec at 4000 rpm, which included a 200 µL toluene wash at 6.5 s during spin coating. After spin coating, the $MAPbI_3$ films were placed under a glass petri dish with 3 µL of DMF to anneal at 65ºC for 5 min and then 100ºC for 10 min. For the Pb-oxysalt passivating layer, an octylammonium sulfate solution was prepared and spin coated directly onto the perovskite layer according to our previous method[101], followed by annealing at 80ºC for 5 min. The $Cs_{.05}(FA_{.83}MA_{.17})_{.95}Pb(I_{.83}Br_{.17})_3$ precursor solution was produced by

dissolving FAI, CsI, MAI, PbI_2, and $PbBr_2$ to yield a 1.2 M solution in a 4:1 ratio DMF:DMSO solution. This precursor was spin coated onto glass slides using the same steps as the $MAPbI_3$ films but that the toluene anti-solvent wash came at 25 s. The films were then annealed according to the annealing steps done to the spin coated $MAPbI_3$ films. The blade coated $MAPbI_3$ thin films were prepared according to our procedure for high-speed, room temperature blading[102]. The $FA_{0.92}Cs_{0.08}PbI_3$ perovskite films were blade coated at room temperature under N_2 knife blowing by using a precursor solution containing 1.0 M $FAPbI_3$ and 0.09 M $CsPbI_3$ dissolved in a 2-Methoxyethanol:DMF solvent mixture. The as-coated solid film was annealed at 150ºC in air for 10 minutes. For all encapsulated films, an epoxy resin was deposited around the edge of the perovskite film and a cover glass slide attached.

All time-resolved photoluminescence measurements were conducted using a FluoTime 300 fluorescence lifetime and steady-state spectrometer (PicoQuant GmbH). A 637 nm pulsed diode laser (PicoQuant LCH-P-C-640B) was used to excite the top side (side exposed to air or cover glass) of each sample; all excitation fluences and repetition rates are stated with their respective figures. Time-resolved emission spectra were recorded by iteratively measuring TRPL from 680 to 860 nm in 2 nm steps (5 nm emission bandpass); the data was acquired for 40 s at each wavelength step. The excitation repetition rate and fluence were 30 kHz and 15 nJ cm^{-2} unless stated otherwise.

2.3 Fluence dependence of Time-resolved Photoluminescence

Polycrystalline $MAPbI_3$ thin films were solution-processed on glass substrates using a one-step spin coating process (see Section 2.2). The TRPL transients of an unencapsulated $MAPbI_3$ film, shown in Figure 2.1a, were measured at several intervals after exposure to air (60% humidity) in the dark for one hour. The times correspond to the duration of exposure to the

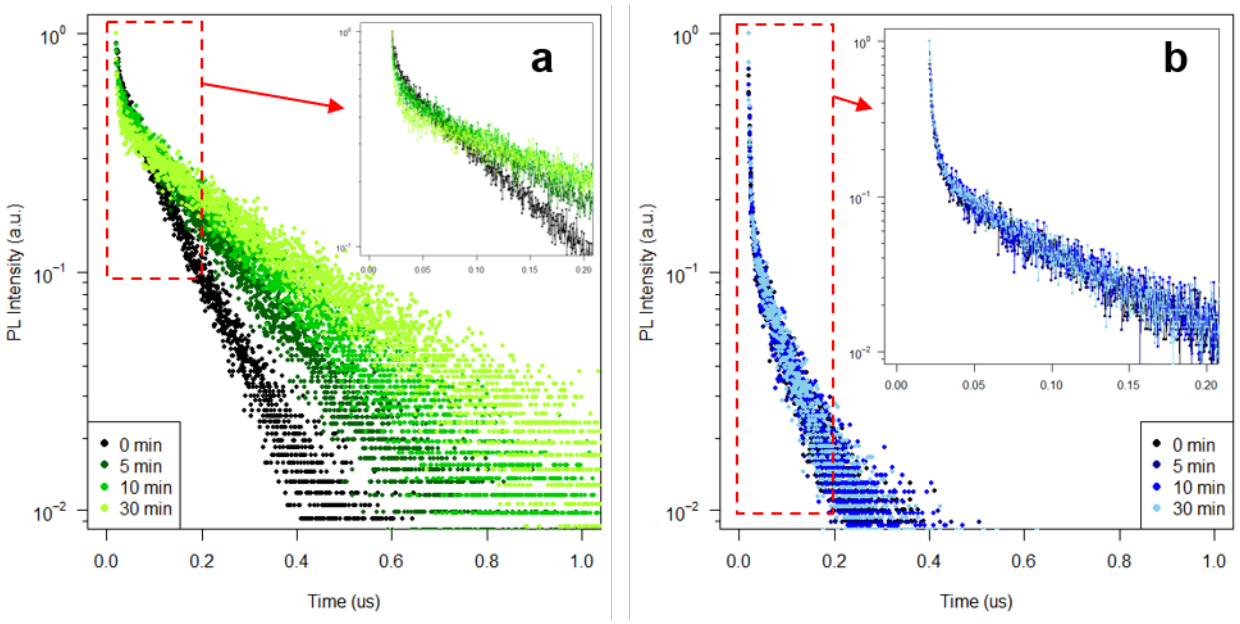

Figure 2.1 Increasing TRPL lifetimes as material degrades. (a) PL transients of a spin-coated $MAPbI_3$ film under continuous 633 nm pulsed excitation in ambient air environment. The times correspond to duration the film has undergone excitation and air exposure before beginning data acquisition. (b) PL transients of an encapsulated $MAPbI_3$ film under continuous pulsed excitation.

pulsed diode laser excitation source at beginning of data acquisition, which was 3 min for each measurement; the excitation fluence was 1.70 nJ cm^{-2}, which corresponds to a carrier concentration of approximately 1.1×10^{14} cm^{-3} for this film. This widely studied composition of metal halide perovskite has repeatedly shown material instability in the presence of moisture[103] and light, yet—as shown in Fig. 1a, we observed an increase in the fluorescence lifetime during the course of that degradation. The inset reveals a distinct biexponential made up of two decays: an initial, fast decay with lifetime decreasing further as the film is exposed to air and light, and a second, slow decay with lifetime that increases during the exposure. In many cases, the long PL decays were misinterpreted as the carrier recombination lifetime, which is not appropriate. In Figure 2.1b, we show the TRPL transients of an encapsulated $MAPbI_3$ film that has undergone identical environmental exposure as the bare perovskite film. With absolutely no change in the recombination dynamics to the protected film, it is clear that the exposed $MAPbI_3$ film in Figure

2.1a has undergone a material change during the pulsed excitation exposure. We speculate that deterioration driven through defects at the grain boundaries and exposed surface of the film produce a high density of traps that manifests itself in the TRPL transients through increased charge trapping and a prolonged detrapping process.

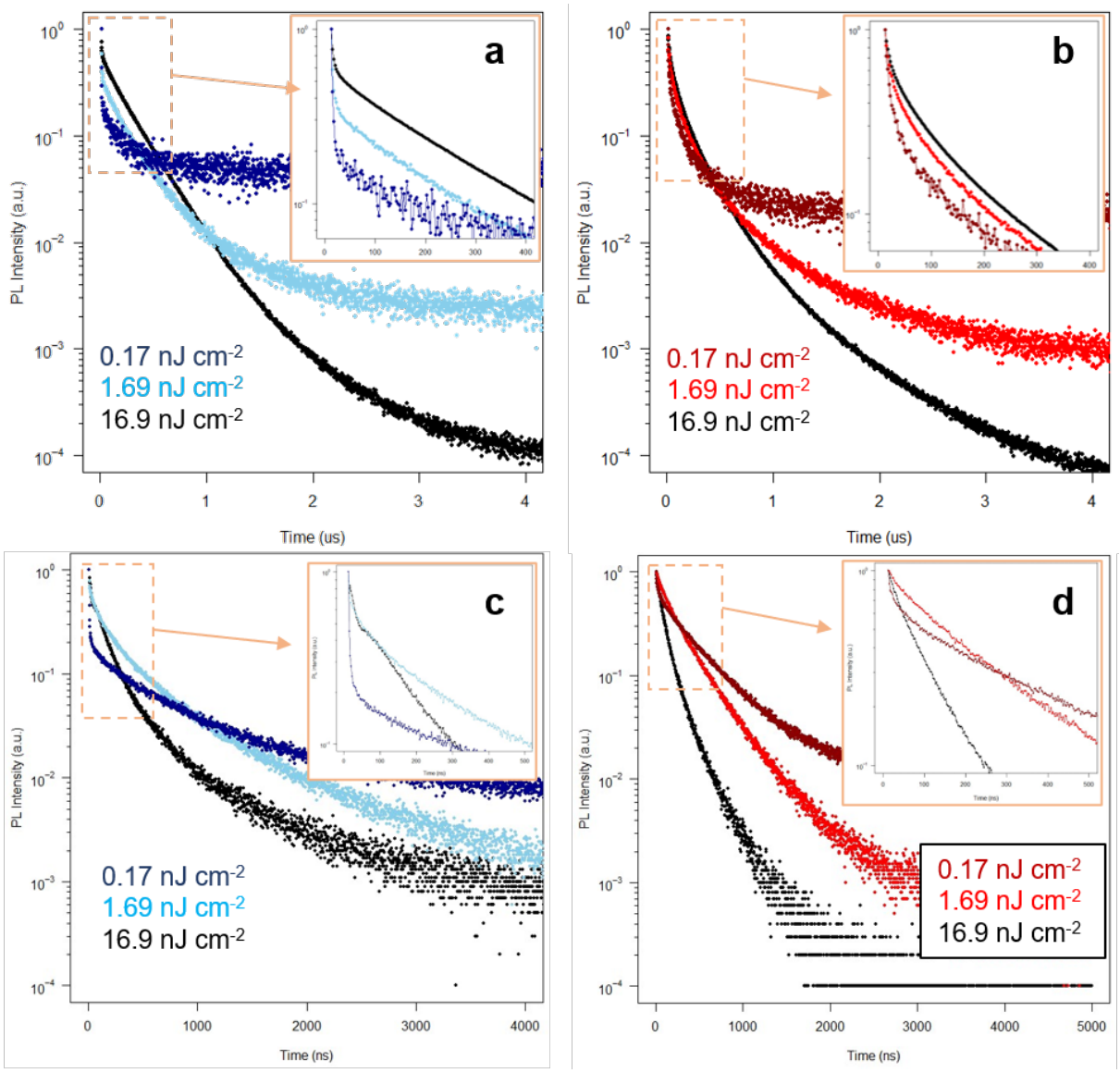

Figure 2.2 Fluence-dependent TRPL of $MAPbI_3$ and triple cation perovskites. Time-resolved PL transients of (a) a neat (i.e. unpassivated) $MAPbI_3$ thin film, (b) an $MAPbI_3$ thin film with a Pb-oxysalt passivating surface layer, (c) a neat $Cs_{.05}(FA_{.83}MA_{.17})_{.95}Pb(I_{.83}Br_{.17})_3$ thin film, and (d) a Pb-oxysalt-passivated $Cs_{.05}(FA_{.83}MA_{.17})_{.95}Pb(I_{.83}Br_{.17})_3$ thin film. Each sample was excited by a 635 nm pulsed diode laser with the same three fluences labeled in each subfigure. Each sample shows pronounced biexponential characteristics (inset) at the lower fluences, particularly the unpassivated films; inset times are in nanoseconds.

To confirm that the observed strong biexponential behavior observed for these low injection levels is dominated by the trapping and detrapping of electrons and holes, we conducted fluence-dependent time-resolved measurements of neat and passivated $MAPbI_3$ and mixed cation and anion perovskite compositions. Looking at Figure 2.2a, the magnitude of the initial fast trapping decay is reduced by increased fluence; this demonstrates that the increased injections levels yield more photoexcited carriers to fill the charge traps and reduce the influence of the trapping behavior[93]. For this film with relatively high defect density (this film was fabricated with no passivating additives or surface layers), we observe that the effects of electron and hole capture have not yet vanished even at the highest fluence of 17 nJ cm^{-2}. Therefore, instead of increasing injection levels, we should expect simply decreasing the number of available trap sites should alleviate the trapping phenomenon. Indeed, as shown in Figure 2.2b, the influence of charge trapping has been greatly reduced at all excitation levels due to the presence of a lead oxysalt passivating layer. This capping layer was shown to reduce defect density by converting the defective surface into a wide bandgap lead oxysalt[39], similar to silicon oxide on silicon. The distinction between the PL transients at different injection levels has been nearly eliminated. Due to decreased levels of trapping sites at the surface of the passivated film, the TRPL measurements have effectively eclipsed the low excitation regime into the stretched exponential decays seen in Figure 2, which are produced by bimolecular recombination and some residual trapping caused by defects within the bulk of the material. It is clear from these figures that the context of the photoexcitation is paramount to the understanding of the resultant PL transients: even with the same injection level used for both the neat and passivated, the relevant recombination processes at play—charge trapping-detrapping and a convolution of the

trap-assisted and bimolecular, respectively—main not remain the same, which should be considered when assessing the quality of the films at hand.

Though $MAPbI_3$ perovskites have been the most widely studied organic-inorganic hybrid perovskite by the community, compositions with mixed cations are fast approaching that moniker due to their strong potential for both high efficiency and stability PSCs[30]. As such, as shown in Figures 2.2c and 2.2d, we observed the same trends in the fluence-dependent transients in an $Cs_{.05}(FA_{.83}MA_{.17})_{.95}Pb(I_{.83}Br_{.17})_3$[30] perovskite composition as the $MAPbI_3$ films. Indeed, the effect appears even more pronounced as shown by the inset of Figure 2.2c; over two orders of magnitude of injection levels, the TRPL measurements go from the strong trapping biexponential form to a faster, nearly monoexponential form with little evidence of the trapping behavior. Figure 2.2d shows the lead oxysalt passivating layer pushes the decays further from the trap-dominated regime of TRPL measurements. To further demonstrate this phenomenon, we performed similar injection level-dependent measurements on a blade-coated $MAPbI_3$ (Figure 2.3) film and a highly stable, methylammonium free $FA_{0.92}Cs_{0.08}PbI_3$ (Figure 2.4) perovskite

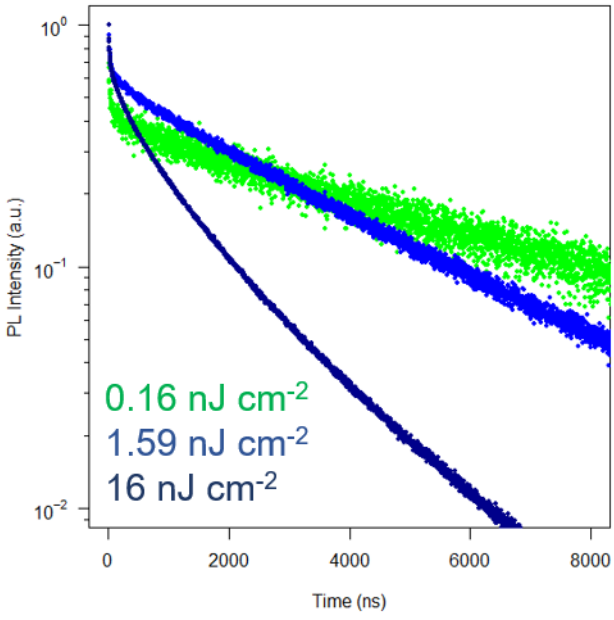

Figure 2.3 PL transients of blade-coated $MAPbI_3$ thin films demonstrate similar trends as spin-coated films. Films were excited by a 635 nm pulsed diode with the same fluences as the spin-coated films in Figure 2.2. The repetition rate was 20 kHz for the lowest fluence and 50 kHz for the rest.

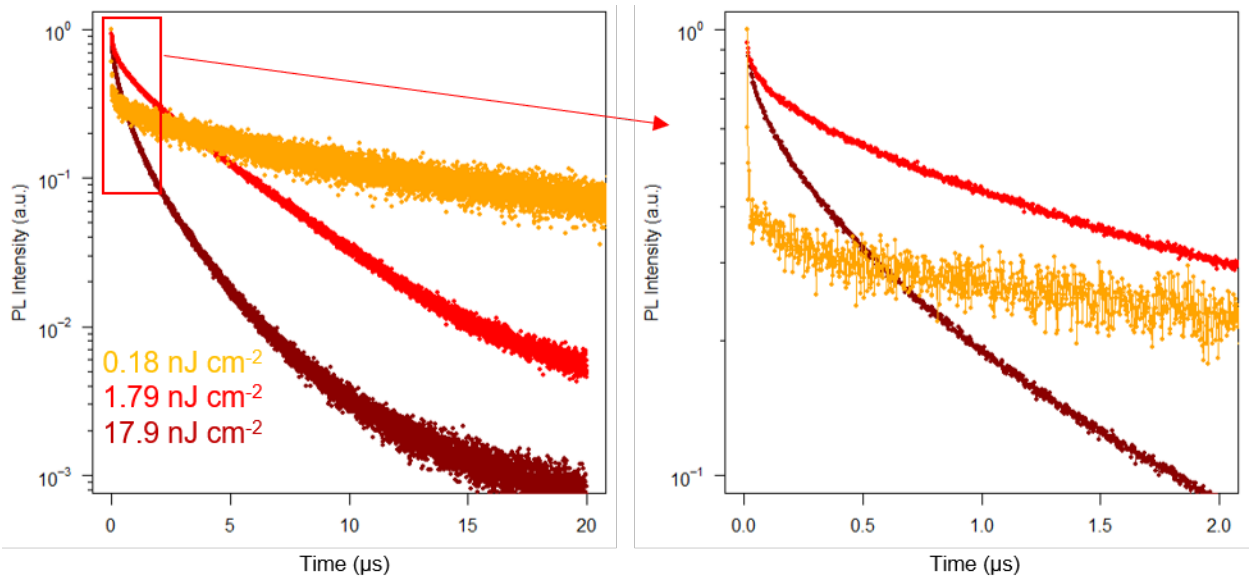

Figure 2.4 Excitation-dependent PL transients of a blade-coated, methylammonium-free $FA_{0.92}Cs_{0.08}PbI_3$ perovskite thin film. This double cation perovskite composition also yields the same excitation dependence as the commonly studied $MAPbI_3$ and triple cation compositions.

film. Both perovskites showed the same characteristic trend of reduced trap dominance due to the increased trap filling of higher injection levels.

2.4 Time-resolved Emission Spectra Reveal Charge Trapping

To further examine the charge trapping process frequently found in these photoluminescence measurements, we conducted time-resolved emission spectroscopy (TRES) on $MAPbI_3$ thin films as shown in Figure 2.5. TRPL decays were measured by sequentially selecting the wavelength of emitted light hitting the detector from 680 to 860 nm (Figure 2.5a). From the array of PL transients, "steady-state" photoluminescence spectra could be constructed at selected time intervals after an excitation pulse from the 637 nm diode laser, as shown in Figure 2.5b. Time zero is designated as the time of the maximum counts from the decay transients. Thus, the TRPL decay manifests itself as the reduction in the intensity of the PL spectra as the time interval becomes further from the time of the excitation pulse. By normalizing the PL spectra in Figure 2.5c, it is clear that the PL peak position and the high energy edge have redshifted over the course of the first few microseconds after an excitation pulse. Immediately

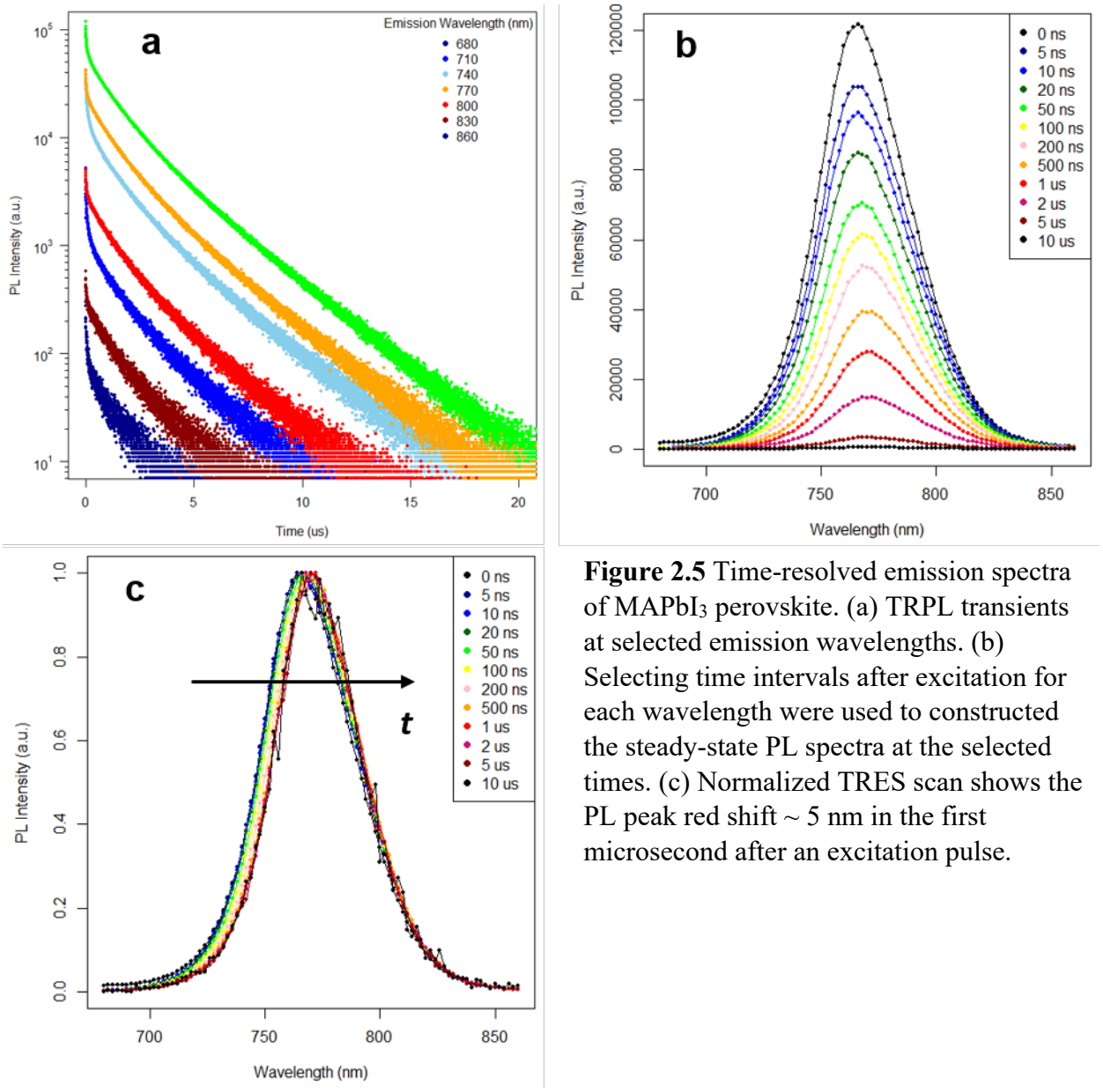

Figure 2.5 Time-resolved emission spectra of $MAPbI_3$ perovskite. (a) TRPL transients at selected emission wavelengths. (b) Selecting time intervals after excitation for each wavelength were used to constructed the steady-state PL spectra at the selected times. (c) Normalized TRES scan shows the PL peak red shift ~ 5 nm in the first microsecond after an excitation pulse.

after excitation at time zero, the center of the PL spectrum lies at 766 nm; after one microsecond, the new center of the PL spectrum has redshifted 5 nm to 771 nm. Considering the strongly biexponential nature of the TRPL transients of the TRES scan, and knowing that electron or hole traps are subgap states that lie below the conduction band and above the valence band, respectively, it is likely that this PL peak redshift is due to the trapping process. If so, we should expect films without sufficient charge trapping to not exhibit such a peak redshift. Indeed, as shown in Figure 2.6a, we observed two $MAPbI_3$ thin films—both unpassivated and passivated

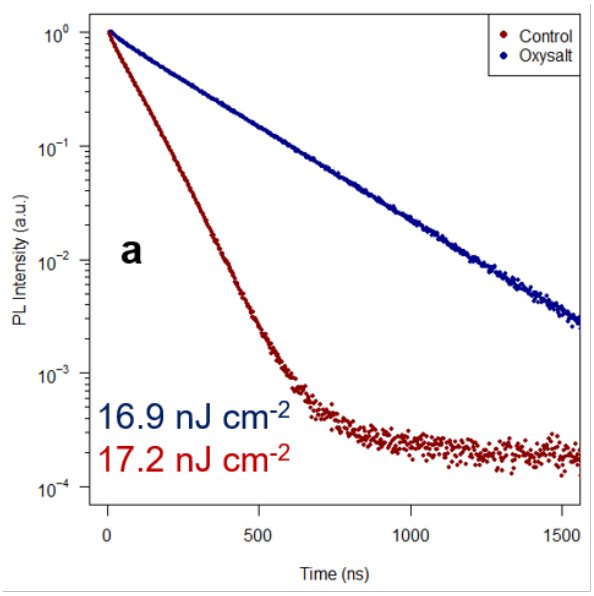

Figure 2.6 TRES of perovskite film without trapping dynamics. a) TRPL transients of neat and lead oxysalt passivated $MAPbI_3$ thin film that do not exhibit trapping behavior. Repetition rates were 0.6 and 0.3 MHz for the neat and passivated films, respectively. The TRES for both (a) the unpassivated and (b) passivated $MAPbI_3$ films show no PL peak shift, due to the lack of trapping dynamics as this fluence.

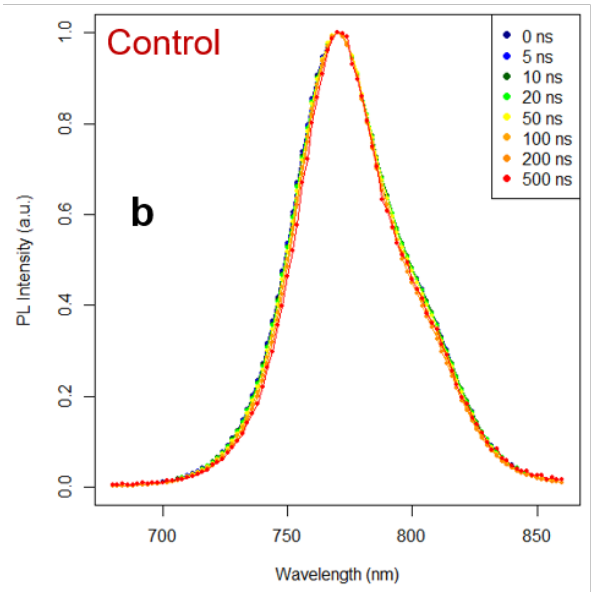

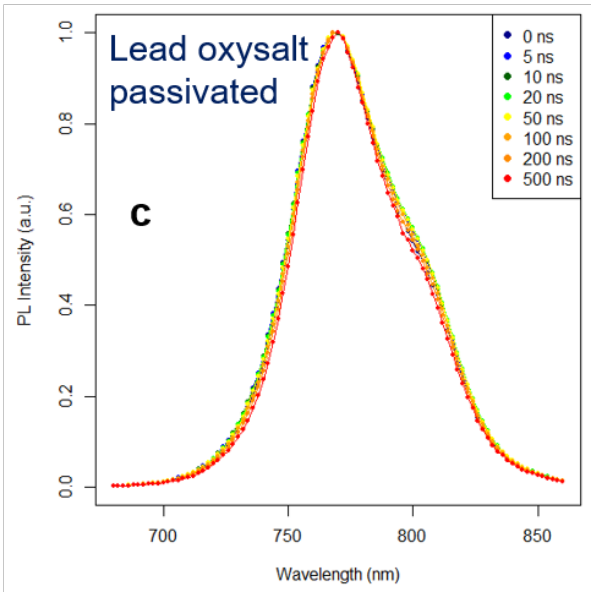

via the Pb-oxysalt technique—that show no evidence of the carrier trapping-detrapping process in their TRPL transients. The passivated film does indeed see an increased carrier lifetime (from ~ 100 to 300 ns) relative to the neat perovskite film due to the decreased defect density by passivated the undercoordinated lead centers at the surface, but neither film demonstrates the characteristic biexponential decay. These films without the trapping behavior both show no PL peak redshift after conducting the time-resolved spectral scans (Figure 2.6b and 2.6c). Both films due, however, exhibit two emission processes: the band-to-band recombination of the $MAPbI_3$

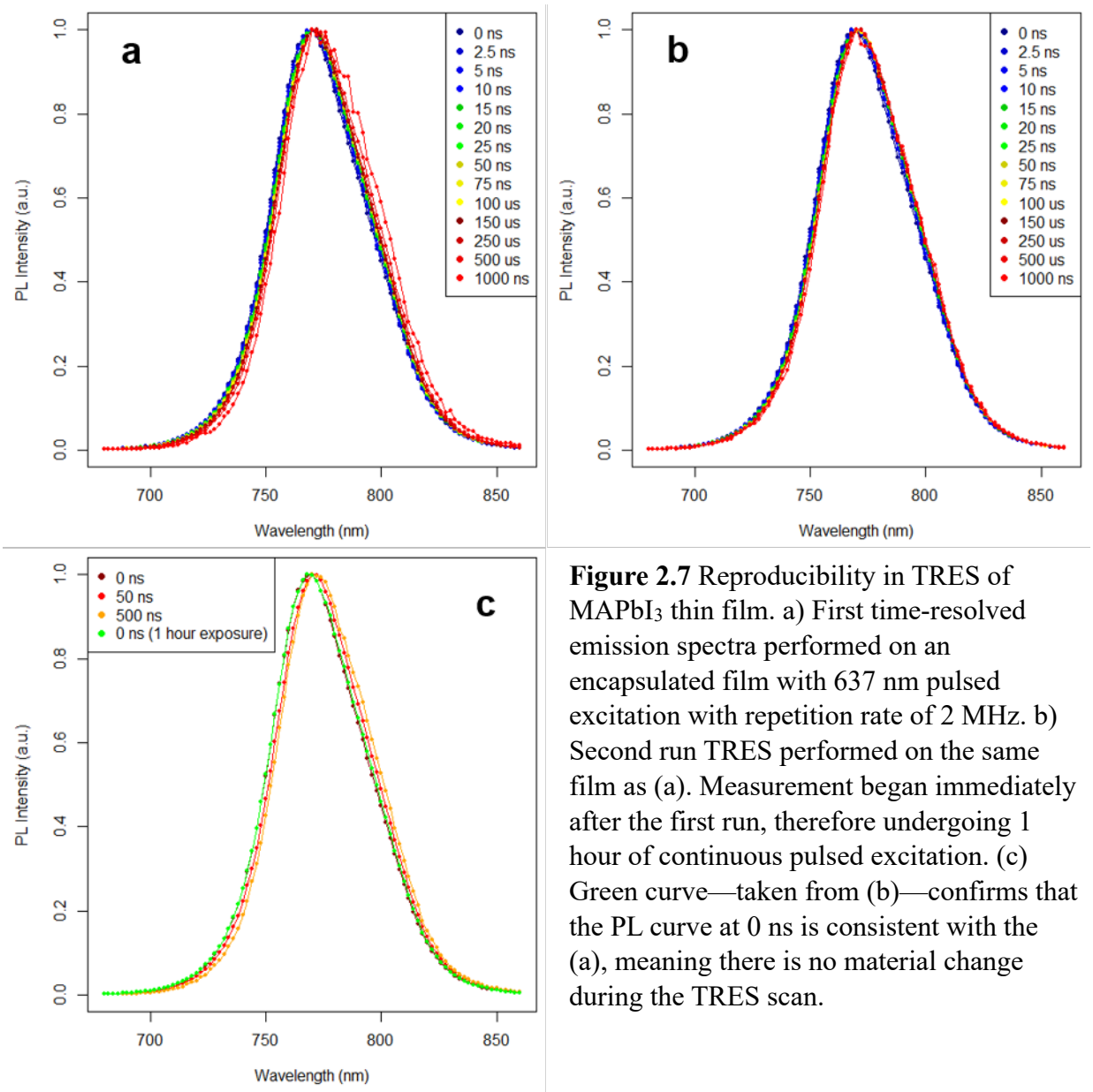

Figure 2.7 Reproducibility in TRES of $MAPbI_3$ thin film. a) First time-resolved emission spectra performed on an encapsulated film with 637 nm pulsed excitation with repetition rate of 2 MHz. b) Second run TRES performed on the same film as (a). Measurement began immediately after the first run, therefore undergoing 1 hour of continuous pulsed excitation. (c) Green curve—taken from (b)—confirms that the PL curve at 0 ns is consistent with the (a), meaning there is no material change during the TRES scan.

around 770 nm, and a second, low energy peak close to 800 nm, which we attribute recombination mediated through PbI_2 at the surface of the perovskite film[104].

As seen in Figure 2.5c, the high energy side and peak of the PL spectra experiences the redshift, whereas the low energy side see little to no shift. It is possible that over the course of the TRES scan, which has the perovskite film endure pulsed illumination for one hour, the film degrades or change in some way during the scan so that the low energy wavelengths do not produce the shift (the scan is conducted from high to low energy—see Section 2.2). To examine

this possibility, we encapsulated all films for the time-resolved emission spectra and ran scans back-to-back. Figures 2.7a and 2.7b show two TRES scans that were executed consecutively; both scans show the same PL peak redshift form. In Figure 2.7c, it is clear that the PL spectra at 0 ns for both run 1 and 2 (maroon and green curves, respectively) overlap, so we can conclude that perovskite degradation is not responsible for the redshift from Figure 2.5.

From Figures 2.6 and 2.7, we can conclude that the charge trapping often observed in TRPL is responsible for the PL peak redshift in time-resolved emission scans. The detrapping of the shallow trap states must come into play as well, as the shift is only 5 nm. For all TRES scans we performed on $MAPbI_3$ thin films, the shift was in this small range of approximately 10-20 meV (for the 5 nm in Figure 2.5, the shift corresponds to 10.5 meV). If the charges were to simply be trapped and then recombine directly from the shallow trap states, then we would expect to see a much larger shift that pushes the emission peak further into the bandgap, well beyond 800 nm[105]. To explain the PL redshift which must be due to both a trapping and detrapping process, we refer to the model in Figure 2.8. Photons are absorbed and electrons (solid blue circles) and holes (hollow red circles) are generated. Charges are concentrated near the surface and their carrier concentration decays exponentially through the depth of the film according to the Beer-Lambert Law. As discuss previously, these charges quickly (much quicker than the timescale of our initial fast trapping process) diffuse. In the low fluence TRPL measurements, many of these charges are quickly trapped by defect states (long dashed lines near the band edges), though some recombine radiatively without ever being first trapped. Before trapping, these charges are distributed within their respective bands, with some electrons and holes extending well beyond the conduction band minimum (CBM) and valence band maximum (VBM), respectively—these are represented by the charges on the left side of the diagram. Once

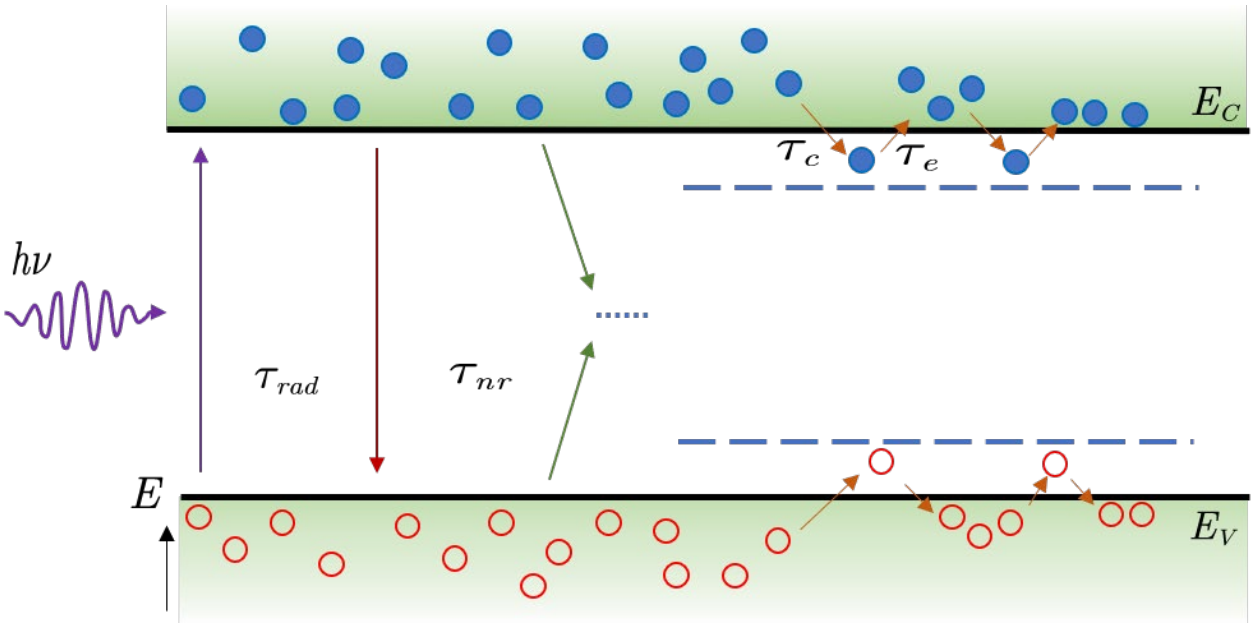

Figure 2.8 Charge Carrier Trapping, Detrapping, and Recombination in MHP. (a) TRPL transients at selected emission wavelengths. (b) Selecting time intervals after excitation for each wavelength were used to constructed the steady-state PL spectra at the selected times. (c) Normalized TRES scan shows the PL peak red shift ~ 5 nm in the first microsecond after an excitation pulse.

trapped, at room temperature, the thermal energy of the charges is sufficient for their reemission band into the carrier bands; however, due to the energy barrier present, the probability of electrons returning higher into the conduction band is lower (the analogous is true for holes). Therefore, over time as free charges are eventually trapped, or trapped charges undergo cycles of capture and emission, the distribution of free carriers in the bands slowly narrows, and the center of that distribution moves toward the CBM and VBM. Thus, the band-to-band emission reduces in energy, which manifests as the small redshift over time in the time-resolved emission spectra. For the individual PL transients for these low fluence experiments, the initial, fast trapping decay is just that; as the charges recombine of the second, longer decay, the rate of emission from the trapped states and of radiative recombination limits the lifetime. Thus, the second decay represents a convolution of these detrapping and radiative processes.

2.5 Conclusion

We have shown that charge trapping is responsible for the strong biexponential behavior present in TRPL decay curves at low excitation fluence. Due to strong charge trapping, PL transient lifetimes can actually be longer due to increased material defects instead of an increase in the charge carrier lifetime of the perovskite. The increased carrier lifetime of these "lower quality" materials is due to the higher density of trap states which quickly capture charges from the carrier before they can radiatively recombine, after they have undergone cycles of capture and thermal emission that redshift the PL spectral peak after an excitation event. Proper understanding of these trapping events and their manifestation in TRPL measurements provides greater insight and accurate assessment of the PL transients.

CHAPTER 3: LARGE-AREA ANTI-REFLECTIVE POLYMER LAYERS FOR EFFICIENT PEROVSKITE SOLAR MODULES

3.1 Introduction

Perovskite solar cells and modules are typically fabricated on TCO/glass substrates with a planar top surface that is the first interface in the device that sunlight encounters. Unfortunately, flat glass surfaces reflect a significant portion of light—particularly if the device is not normal to the incident photons—which lead to significant losses in PCE due to nonoptimal photon absorption. Textured absorber interfaces (a random distribution of pyramids) within a silicon device stack, as well as textured polydimethylsiloxane (PDMS) polymer scattering layers have been shown to reduce these losses in small scale (< 1 cm^2) perovskite solar cells[75]. Increases in photovoltaic efficiency largely manifest from increased short-circuit current density because of the higher number of absorbed photons for a given device area.

The commercialization of PSCs, however, requires scalable fabrication methods to manufacture solar modules quickly while maintaining the high efficiencies of laboratory scale solar cells. This includes are elements of the PSC fabrication process, including top surface anti-reflective layers. In this work, we scale the fabrication of polydimethylsiloxane (PDMS) scattering layers for use with $MAPbI_3$ perovskite mini-modules (over 50 cm^2) and demonstrate increased J_{SC} and PCE in these large area perovskite devices. The PDMS scattering layers were optimized by controlling textured substrate morphology and layer thickness. The champion anti-reflection layer boosted module J_{SC} and PCE from 19.78 mA cm^{-2} and 14.71% to 20.99 mA cm^{-2} and 16.32%, respectively. External quantum efficiency (EQE) measurements of small-scale

PSCs with and without PDMS scattering layers confirmed improved light management. In addition to the textured silicon substrate method, we demonstrated the ability to fabricate PDMS scattering layers using a Blu-ray movie disc, whose quasi-random surface has been shown to provide nearly optimal light management across the visible light spectrum[106]. These PDMS layers made from the Blu-ray disc template effectively increased light harvesting in small area PSCs, increasing the device J_{SC} by an average of 6.3%—relative to 4.4% for the scattering layers from the textured silicon template. Though mini-module-sized scattering layers could not be produced from the Blu-ray discs, their performance for the small area devices was impressive, and the potential for scalable production already exists.

3.2 Device and Scattering Layer Fabrication

Perovskite modules were prepared on prepatterned ITO/glass substrates, which were washed with detergent, isopropanol, and acetone sequentially. After a 15-minute UV-ozone treatment, 5 mg/ml of PTAA in toluene was blade coated at 19 mm/s with a 200-µm blade height. Next, the perovskite layer was blade-coated at room temperature using an air knife for its high-speed, low temperature capabilities[102]. A 1.0 M $MAPbI_3$ solvent (3:2 volume ratio of

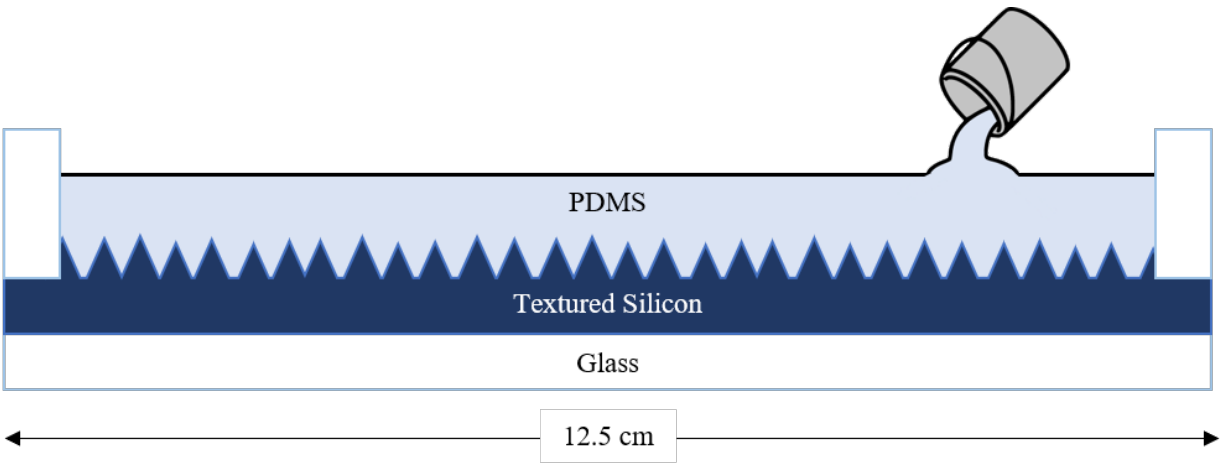

Figure 3.1 Schematic of fabrication of the PDMS scattering layer. The polymer mixture is poured extremely slowly to evenly cover the large area substrate and prevent the formation of bubbles.

acetonitrile and 2-Methoxyethanol) was coated at 99 mm/s with a 250 μm blade height. Additives to improve device performance were added to the solution according to reference [102]. The perovskite film was annealed at 70ºC for approximately 5 minutes and then at 100ºC for 10 minutes. After annealing, 30 nm of C_{60} and 6 nm of BCP were thermally evaporated. To create the monolithic perovskite module, laser scribing was performed before and after Cu electrode deposition according to reference 17. The final aperture area of the module was 57 cm^2, which includes the dead zones of the serial connections between subcells.

PDMS scattering layers were fabricated on 12.5 cm by 12.5 cm silicon wafers, textured with micrometer scale pyramids (see reference 75). Using Sylgard 184 from Dow Corning, 15 mL of base and 1.5 mL of curing agent were mixed and diluted with 2.25 mL toluene (10:1 weight ratio). This mixture was then degassed via ultrasonication then dispensed onto the textured silicon substrate (see Figure 3.1) that had been soaked in toluene for 1 min. The PDMS was poured slowly onto the wafer to cover the entire surface with a few millimeters of the mixture to give the resultant polymer layer with approximately 1 mm thickness. The PDMS was cured at 46ºC for 12 hr and then slowly separated from the substrate to produce the negative of the textured template.

3.3 Efficiency Enhancement by Improved Photon Collection

PSC Modules with PDMS Anti-reflection Layers

The random pyramid structure of the PDMS layers created by the textured silicon change the top surface our perovskite surfaces modules from a planar glass surface to a micro-scale textured surface that scatters incoming light into the cell and mitigates the reflection losses of the planar surface. A schematic of a subcell of a perovskite module (i.e. the series connections of the module are not depicted) is shown in Figure 3.2a with the polymer scattering layer applied to the

top surface. To determine change in reflectance at a normal incidence due to the scattering layer, the reflectance of both a bare perovskite module and module with PDMS layer were measured using a PerkinElmer LAMBDA 1050+ UV/Vis/NIR spectrophotometer. As shown in Figure 3.2b, the presence of the PDMS anti-reflection layer reduced the reflectance across the entire spectrum relevant to photovoltaics by approximating 2-3% (in absolute reflectance) depending

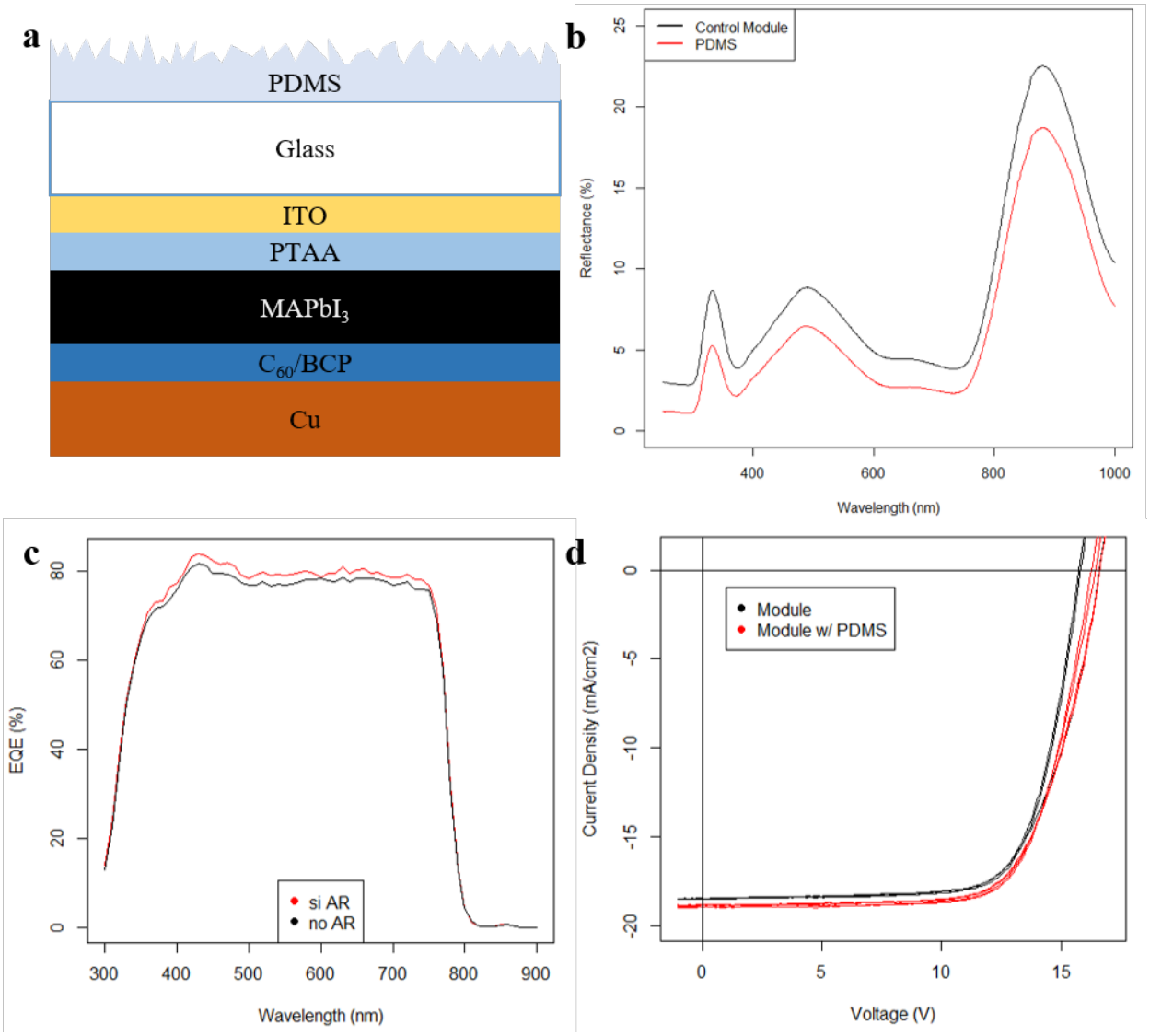

Figure 3.2 (a) Schematic of PSC stack with PDMS scattering layer. **(b)** Absolute reflectance of perovskite module with planar glass (black) and PDMS anti-reflective (red) top surfaces. **(c)** External quantum efficiency of an $MAPbI_3$ module with and without an anti-reflective PDMS layer fabricated from the textured Si template. **(d)** J-V curves of the $MAPbI_3$ module with a scattering layer show improved photovoltaic performance.

on the wavelength. By observing different regions of the PDMS covered module, we found that there were no regions in which the scattering layer did not decrease the reflectance relative to the planar glass surface.

To confirm the reduced reflection translated to improved device performance, we measured the EQE and J-V characteristics of a perovskite solar module with and without the PDMS scattering layer, which are shown in Figure 3.2c and 3.2d, respectively. The EQE of an $MAPbI_3$ module with the anti-reflection layer produced from the Si template is increased by approximately 3-4% points in the range from 400 to 800 nm. This correlated to the increase in short circuit current seen in Figure 3.2d, where the average J_{SC} increased from 18.5 mA cm^{-2} in control modules to 18.9 mA cm^{-2} in PDMS covered modules (a 2.2% increase). Combined with the increase to the V_{OC} of the modules, the PCE increases from 12.73% to 13.15% with the presence of the PDMS scattering layer. Figure 3.3 shows a perovskite module with and without the polymer scattering layer after it has been exposed to air and light for several hours; all J-V measurements were recorded prior to any signs of degradation.

Micro-scale Texture Optimization

To increase the efficacy of the large-area polymer scattering layers for perovskite solar modules, we sought to control both the morphology of the micro-scale texture responsible for the light scattering and the thickness of the PDMS layer. First, we used two separate textured silicon substrates with different characteristic dimensions of the pyramid features. Both substrates had the same random pyramid features on the scale of micrometers, but we found that PDMS anti-reflection layers with pyramid features of 2-5 μm size (green curves) yielded better light management than layers with features that were 1 μm or smaller (blue curves). Figure 3.4a

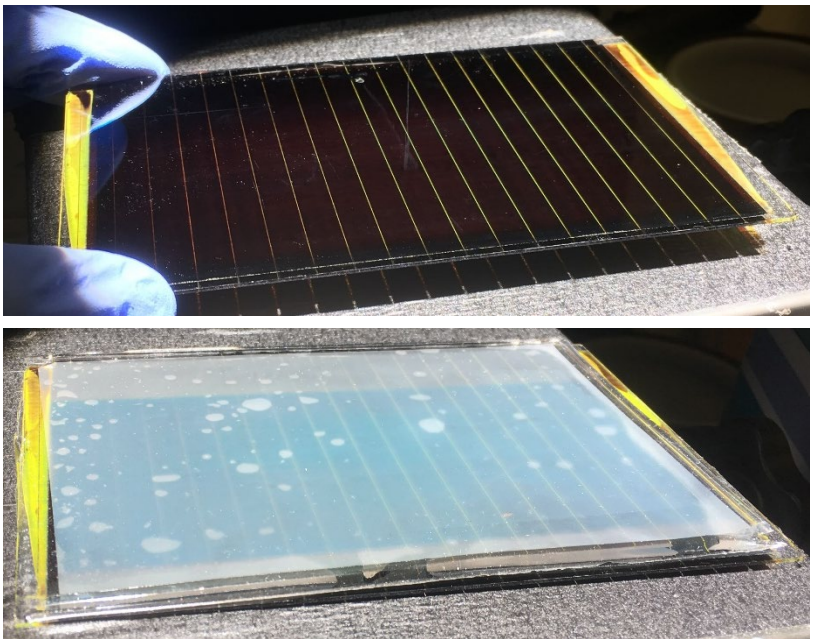

Figure 3.3 Perovskite solar module with and without a PDMS scattering layer. The anti-reflection layer was carefully applied and all large bubbles removed for device testing. This device shows yellow perovskite phase where the film was exposed to air (i.e. not covered by the Cu electrode), which appears after several hours exposed to air and light.

shows that the larger pyramid structures increased the J_{SC} by over 1 mA cm^{-2} relative to the smaller featured PDMS layer, which was an even greater increase than we saw previous from control (black curve) to PDMS covered module. The size of the textured silicon pyramids had no effect on the fabrication or removal of the PDMS layer from the template, and both could be equally made to uniform thickness.

Another aspect of the PDMS layer that could be controlled was its thickness. The layer needed to be thick enough that it could be reliably removed from the silicon substrate (approximately 1 mm was as thin possible for this requirement), but otherwise the thickness could be tuned by changing the volume of the Sylgard 184 mixture applied to the textured silicon. However, we found no appreciable difference in the J_{SC}, V_{OC}, or PCE of a perovskite module when the thickness of the PDMS layer was tuned. Figure 3.4a shows the J-V curves of PDMS layers with 1.1 mm (green curves) and 0.9 mm (red curves) thickness, and multiple layers of each respective thickness showed that the thickness of the layer was a nonfactor in the improvement of light management relative to the size of the micro-scale texture.

To further explore the effects of the morphology template used for polymer scattering layer fabrication, we turned to a well-known product that has already realize mass production of quasi-random nanostructures. Smith et al. demonstrated the repurposing of Blu-ray discs to imprint their nano-scale structure onto the active layer of polymer solar cells, which yielded high absorption and PCE. The compression algorithms used to efficiently store the audio and video data onto the disc create a high-entropy binary sequence that is printed onto the disc, producing a quasi-random series of valleys. To use the Blu-ray nanostructures as a template for our PDMS scattering layers, we removed the protective optical transmission layer from the bottom of a Blu-ray movie disc to reveal the nanostructures, and then proceeded with the PDMS fabrication as before.

The PDMS scattering layer produced from the Blu-ray disc was considerably smaller than our large-area layers produced for the perovskite modules—due to the limitations of the size

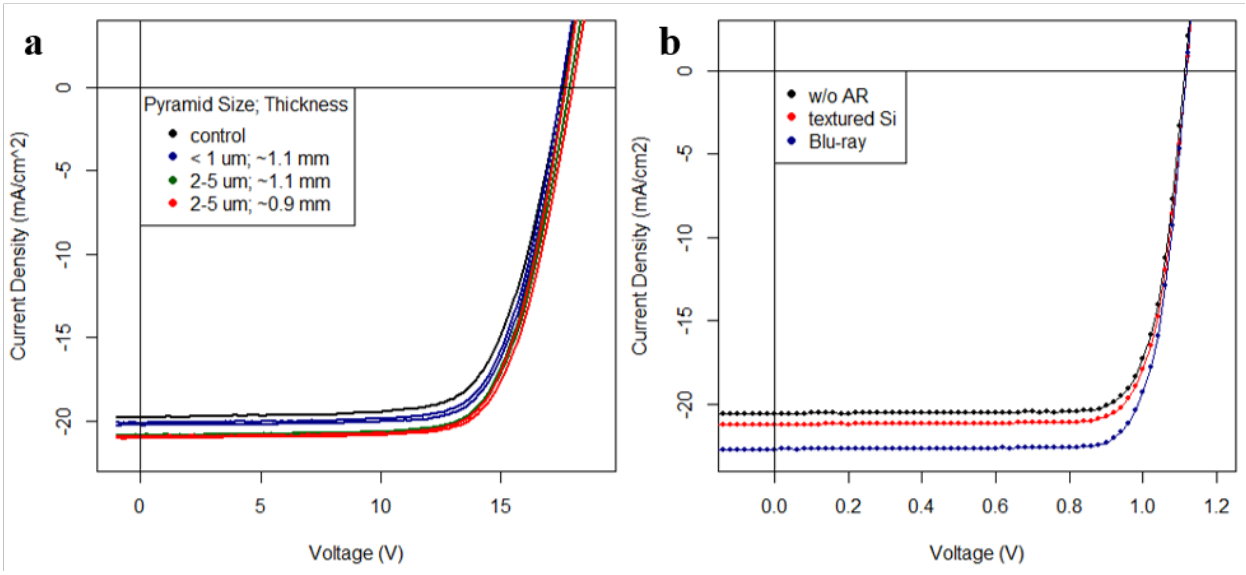

Figure 3.4 Improving PCE by controlling PDMS surface morphology. **(a)** J-V curves of perovskite solar modules comparing small (blue) and large (green) pyramid features, thick (green) and thin (red) PDMS layers, and a control planar glass top surface. **(b)** J-V curves of small-area PSCs with PDMS layers fabricated from textured silicon (red) and Blu-ray disc templates.

and shape of the disc—and thus were tested on small, 8 mm^2 PSCs. To compare the Blu-ray and textured silicon morphologies, we observed the J-V characteristics of a $MAPbI_3$ solar cell while using the PDMS layers produced from the two templates. While the textured silicon substrate improved the short circuit current again by 1 mA cm^{-2}, the PDMS fabricated from the Blu-ray nanostructures increased the J_{SC} by an impressive 3 mA cm^{-2} (Figure 3.4b).

3.4 Conclusion

We demonstrated the fabrication of large-area PDMS scattering layers optimized to improve light management in perovskite solar modules, thereby increasing photon absorption to boost short circuit current and PCE. Textured silicon with random pyramid features larger (2-5 μm) than the wavelength of the visible spectrum was shown to produce a more effective PDMS scattering layer than using features that were smaller and comparable to the wavelengths of light being scattered. We utilized the quasi-random structure of Blu-ray movie discs[106] as another template to fabricate PDMS scattering layers for small-area PSCs, and confirmed their photon management capabilities could be translated to the anti-reflective polymer surface. Further work could see the fabrication of large-scale polymer scattering layers larger than 100 cm^2 for the Blu-ray nanostructures by utilizing their large-scale production capability, which could boost the PCE of perovskite modules to new heights.

CHAPTER 4: SUMMARY AND OUTLOOK

The work of this thesis focused on the recombination dynamics present when studying metal halide perovskites for photovoltaic applications. The research presented here enhanced the understanding of time-resolved photoluminescence measurements in hybrid perovskites, which is critical for the development of novel compositions and passivating techniques that lower nonradiative recombination and increase the efficiency of PSCs. The efforts with anti-reflective polymer scattering layers also enhances PCE by increasing light absorbed in larger-scale perovskite solar modules.

Low excitation power TRPL was studied to probe the effects of charge trapping on the PL transient lifetimes and the manifestation of biexponential decays. We observed that charge trapping can increase TRPL lifetimes, which are typically associated with improved carrier lifetime and thus film quality. The characteristic biexponential TRPL decays and the spectral redshift that occurred after photoexcitation could be explained by the cyclic trapping, detrapping, and recombination processes at play in the MHP thin films.

Anti-reflective PDMS polymer layers were scaled to the size of perovskite solar modules, increasing the short circuit current and PCE of devices greater than 50 cm^2. Changes to the morphology of the templates used to fabricate the PDMS scattering layers improved their light management capabilities. Scattering pyramids larger than the wavelength of the visible spectrum increased the J_{SC} by 4% relative to pyramids with characteristic sizes comparable to the wavelength of light being scattered. Additionally, we utilized the optimized light scattering properties of Blu-ray disc nanostructures to improve the PCE of PSCs.

Though the efficiency of PSCs has skyrocketed to beyond 25% in just a decade of intense study, a significant gap between the efficiency of the best perovskite devices and the SQ limit remains, and nonradiative, trap-mediated recombination due to material defects remains a major culprit. These defects are also the source for the greatest roadblock to PSC commercialization: stability. Despite efforts on device encapsulation (which does indeed greatly increase functional lifetime), all of the highest efficiency perovskite compositions—particularly compositions with the ideal bandgap to meet the SQ limit—are intrinsically unstable. Work is needed to better understand the nonradiative recombination mechanisms in PSCs so that they may be better passivated. Additionally, addressing the issues of large-scale fabrication methods and the toxicity of lead, the most widely used B-site cation, also provide significant challenges to the perovskite community.

REFERENCES

1. Miyasaka, T., Kojima, A., Teshima, K. & Shirai, Y. Organometal halide perovskites as visible-light sensitizers for photovoltaic cells. *J. Am. Chem. Soc.* **131**, 6050–6051 (2009).

2. Tan, Z. K. *et al.* Bright light-emitting diodes based on organometal halide perovskite. *Nat. Nanotechnol.* **9**, 687–692 (2014).

3. Wei, H. *et al.* Sensitive X-ray detectors made of methylammonium lead tribromide perovskite single crystals. *Nat. Photonics* **10**, 333 (2016).

4. Wei, H. *et al.* Dopant compensation in alloyed CH3NH3PbBr3−xClx perovskite single crystals for gamma-ray spectroscopy. *Nat. Mater.* **16**, 826 (2017).

5. Xiao, Z. & Huang, J. Energy-Efficient Hybrid Perovskite Memristors and Synaptic Devices. *Adv. Electron. Mater.* **2**, 1–8 (2016).

6. National Renewable Energy Laboratory. PV Research Cell Record Efficiency Chart. *Natl. Renew. Energy Lab.* (2020).

7. Lee, T. D. & Ebong, A. U. A review of thin film solar cell technologies and challenges. *Renewable and Sustainable Energy Reviews* (2017) doi:10.1016/j.rser.2016.12.028.

8. Solar Frontier. Solar Frontier Achieves World Record Thin-Film Solar Cell Efficiency of 23.35%. 1–2 http://www.solar-frontier.com/eng/news/2019/0117_press.html (2019).

9. Hu, M., Bi, C., Yuan, Y., Bai, Y. & Huang, J. Stabilized wide bandgap MAPbBrxI3-xperovskite by enhanced grain size and improved crystallinity. *Adv. Sci.* (2015) doi:10.1002/advs.201500301.

10. McMeekin, D. P. *et al.* A mixed-cation lead mixed-halide perovskite absorber for tandem solar cells. *Science (80-.).* **351**, 151–155 (2016).

11. Jaysankar, M. *et al.* Perovskite-silicon tandem solar modules with optimised light harvesting. *Energy Environ. Sci.* (2018) doi:10.1039/c8ee00237a.

12. Sahli, F. *et al.* Fully textured monolithic perovskite/silicon tandem solar cells with 25.2% power conversion efficiency. *Nat. Mater.* (2018) doi:10.1038/s41563-018-0115-4.

13. Deng, Y. *et al.* Scalable fabrication of efficient organolead trihalide perovskite solar cells with doctor-bladed active layers. *Energy Environ. Sci.* (2015) doi:10.1039/c4ee03907f.

14. Barrows, A. T. *et al.* Efficient planar heterojunction mixed-halide perovskite solar cells deposited via spray-deposition. *Energy Environ. Sci.* (2014) doi:10.1039/c4ee01546k.

15. Hwang, K. *et al.* Toward large scale roll-to-roll production of fully printed perovskite solar cells. *Adv. Mater.* (2015) doi:10.1002/adma.201404598.

16. Kim, J. H., Williams, S. T., Cho, N., Chueh, C. C. & Jen, A. K. Y. Enhanced Environmental Stability of Planar Heterojunction Perovskite Solar Cells Based on Blade-Coating. *Adv. Energy Mater.* (2015) doi:10.1002/aenm.201401229.

17. Deng, Y. *et al.* Surfactant-controlled ink drying enables high-speed deposition of perovskite films for efficient photovoltaic modules. *Nat. Energy* (2018) doi:10.1038/s41560-018-0153-9.

18. De Wolf, S. *et al.* Organometallic halide perovskites: Sharp optical absorption edge and its relation to photovoltaic performance. *J. Phys. Chem. Lett.* (2014) doi:10.1021/jz500279b.

19. Hao, F., Stoumpos, C. C., Cao, D. H., Chang, R. P. H. & Kanatzidis, M. G. Lead-free solid-state organic-inorganic halide perovskite solar cells. *Nat. Photonics* **8**, 489–494 (2014).

20. Tanaka, K. *et al.* Comparative study on the excitons in lead-halide-based perovskite-type crystals CH3NH3PbBr3 CH3NH 3PbI3. *Solid State Commun.* (2003) doi:10.1016/S0038-1098(03)00566-0.

21. D'Innocenzo, V. *et al.* Excitons versus free charges in organo-lead tri-halide perovskites. *Nat. Commun.* (2014) doi:10.1038/ncomms4586.

22. Herz, L. M. Charge-Carrier Dynamics in Organic-Inorganic Metal Halide Perovskites. *Annu. Rev. Phys. Chem.* (2016) doi:10.1146/annurev-physchem-040215-112222.

23. Stranks, S. D. *et al. Electron-Hole Diffusion Lengths Exceeding 1 Micrometer in an Organometal Trihalide Perovskite Absorber Downloaded from*. *www.sciencemag.org SCIENCE* vol. 342 http://science.sciencemag.org/ (2013).

24. Wehrenfennig, C., Eperon, G. E., Johnston, M. B., Snaith, H. J. & Herz, L. M. High charge carrier mobilities and lifetimes in organolead trihalide perovskites. *Adv. Mater.* (2014) doi:10.1002/adma.201305172.

25. Shi, D. *et al. Low trap-state density and long carrier diffusion in organolead trihalide perovskite single crystals*. vol. 347 http://science.sciencemag.org/ (2015).

26. Dequilettes, D. W. *et al.* Impact of microstructure on local carrier lifetime in perovskite solar cells. *Science (80-.).* **348**, 683–686 (2015).

27. Dong, Q. *et al.* Electron-hole diffusion lengths > 175 μm in solution-grown CH3NH3PbI3 single crystals. *Science (80-.).* (2015) doi:10.1126/science.aaa5760.

28. Bi, Y. *et al.* Charge Carrier Lifetimes Exceeding 15 μs in Methylammonium Lead Iodide Single Crystals. *J. Phys. Chem. Lett.* (2016) doi:10.1021/acs.jpclett.6b00269.

29. Steirer, K. X. *et al.* Defect Tolerance in Methylammonium Lead Triiodide Perovskite. *ACS Energy Lett.* (2016) doi:10.1021/acsenergylett.6b00196.

30. Saliba, M. *et al.* Cesium-containing triple cation perovskite solar cells: Improved stability, reproducibility and high efficiency. *Energy Environ. Sci.* **9**, 1989–1997 (2016).

31. Shockley, W. & Queisser, H. J. Detailed balance limit of efficiency of p-n junction solar cells. *J. Appl. Phys.* (1961) doi:10.1063/1.1736034.

32. Shaklee, K. L. & Nahory, R. E. Valley-Orbit Splitting of Free Excitons? the Absorption Edge of Si. *Phys. Rev. Lett.* **24**, 942–945 (1970).

33. Fehrenbach, G., Schaefer, W. & Ulbrich, R. Excitonic versus plasma screening in highly excited gallium arsenide. *J. Lumin.* **30**, 154–161 (1985).

34. Bakulin, A. A. *et al.* The Role of Driving Energy and Delocalized States for Charge Separation in Organic Semiconductors. *Science (80-.).* **335**, 1340–1344 (2012).

35. Gélinas, S. *et al.* The Binding Energy of Charge-Transfer Excitons Localized at Polymeric Semiconductor Heterojunctions. *J. Phys. Chem.* **115**, 7114–7119 (2011).

36. Savenije, T. J. *et al.* Thermally activated exciton dissociation and recombination control the carrier dynamics in organometal halide perovskite. *J. Phys. Chem. Lett.* **5**, 2189–2194 (2014).

37. Sun, S. *et al.* The origin of high efficiency in low-temperature solution-processable bilayer organometal halide hybrid solar cells. *Energy Environ. Sci.* **7**, 399–407 (2014).

38. Hu, M. *et al.* Distinct exciton dissociation behavior of organolead trihalide perovskite and excitonic semiconductors studied in the same system. *Small* **11**, 2164–2169 (2015).

39. Giebink, N. C., Wiederrecht, G. P., Wasielewski, M. R. & Forrest, S. R. Thermodnamic efficiency limit of excitonic solar cells. *Phys. Rev. B* (2011) doi:10.1103/PhysRevB.83.195326.

40. Johnston, M. B. & Herz, L. M. Hybrid Perovskites for Photovoltaics: Charge-Carrier Recombination, Diffusion, and Radiative Efficiencies. *Acc. Chem. Res.* (2016) doi:10.1021/acs.accounts.5b00411.

41. Davies, C. L. *et al.* Bimolecular recombination in methylammonium lead triiodide perovskite is an inverse absorption process. *Nat. Commun.* (2018) doi:10.1038/s41467-017-02670-2.

42. Ball, J. M. & Petrozza, A. Defects in perovskite-halides and their effects in solar cells. *Nat. Energy* **1**, (2016).

43. Pazos-Outón, L. M., Xiao, T. P. & Yablonovitch, E. Fundamental Efficiency Limit of Lead Iodide Perovskite Solar Cells. *Journal of Physical Chemistry Letters* (2018) doi:10.1021/acs.jpclett.7b03054.

44. Shockley, W. & Read, W. T. Statistics of the Recombinations of Holes and Electrons.

Phys. Rev. **87**, 835–842 (1952).

45. Yamada, Y., Nakamura, T., Endo, M., Wakamiya, A. & Kanemitsu, Y. Photocarrier recombination dynamics in perovskite CH3NH3PbI3for solar cell applications. *J. Am. Chem. Soc.* (2014) doi:10.1021/ja506624n.

46. Milot, R. L., Eperon, G. E., Snaith, H. J., Johnston, M. B. & Herz, L. M. Temperature-Dependent Charge-Carrier Dynamics in CH3NH3PbI3Perovskite Thin Films. *Adv. Funct. Mater.* (2015) doi:10.1002/adfm.201502340.

47. Ponseca, C. S. *et al.* Organometal halide perovskite solar cell materials rationalized: Ultrafast charge generation, high and microsecond-long balanced mobilities, and slow recombination. *J. Am. Chem. Soc.* **136**, 5189–5192 (2014).

48. Stranks, S. D. *et al.* Recombination Kinetics in Organic-Inorganic Perovskites: Excitons, Free Charge, and Subgap States. *Phys. Rev. Appl.* (2014) doi:10.1103/PhysRevApplied.2.034007.

49. Kim, J., Lee, S. H., Lee, J. H. & Hong, K. H. The role of intrinsic defects in methylammonium lead iodide perovskite. *J. Phys. Chem. Lett.* **5**, 1312–1317 (2014).

50. Zhu, K., Miyasaka, T., Kim, J. Y. & Mora-Seró, I. Trend of perovskite solar cells: Dig deeper to build higher. *J. Phys. Chem. Lett.* **6**, 2315–2317 (2015).

51. Xiao, Z. *et al.* Solvent Annealing of Perovskite-Induced Crystal Growth for Photovoltaic-Device Efficiency Enhancement. *Adv. Mater.* (2014) doi:10.1002/adma.201401685.

52. Noel, N. K. *et al.* Enhanced photoluminescence and solar cell performance via Lewis base passivation of organic-inorganic lead halide perovskites. *ACS Nano* **8**, 9815–9821 (2014).

53. Stranks, S. D. & Snaith, H. J. Metal-halide perovskites for photovoltaic and light-emitting devices. *Nature Nanotechnology* (2015) doi:10.1038/nnano.2015.90.

54. Yin, W. J., Shi, T. & Yan, Y. Unique properties of halide perovskites as possible origins of the superior solar cell performance. *Adv. Mater.* (2014) doi:10.1002/adma.201306281.

55. Yang, M. *et al.* Do grain boundaries dominate non-radiative recombination in CH3NH3PbI3perovskite thin films? *Phys. Chem. Chem. Phys.* (2017) doi:10.1039/c6cp08770a.

56. Reid, O. G., Yang, M., Kopidakis, N., Zhu, K. & Rumbles, G. Grain-Size-Limited Mobility in Methylammonium Lead Iodide Perovskite Thin Films. *ACS Energy Lett.* **1**, 561–565 (2016).

57. Stranks, S. D. Nonradiative Losses in Metal Halide Perovskites. *ACS Energy Letters* (2017) doi:10.1021/acsenergylett.7b00239.

58. Han, Q. *et al.* Single Crystal Formamidinium Lead Iodide (FAPbI 3): Insight into the

Structural, Optical, and Electrical Properties. *Adv. Mater.* (2016) doi:10.1002/adma.201505002.

59. Maiberg, M., Hölscher, T., Zahedi-Azad, S. & Scheer, R. Theoretical study of time-resolved luminescence in semiconductors. III. Trap states in the band gap. *J. Appl. Phys.* (2015) doi:10.1063/1.4929877.

60. Saliba, M. *et al.* Incorporation of rubidium cations into perovskite solar cells improves photovoltaic performance. *Science (80-.).* **354**, (2016).

61. Silver-Hamill Turren-Cruz, Anders Hagfeldt, M. S. Methylammonium-free, high-performance and stable perovskite solar cells on a planar architecture. *Science (80-.).* (2018).

62. Yi, C. *et al.* Entropic stabilization of mixed A-cation ABX3metal halide perovskites for high performance perovskite solar cells. *Energy Environ. Sci.* (2016) doi:10.1039/c5ee03255e.

63. Wang, Z. *et al.* Efficient and Air-Stable Mixed-Cation Lead Mixed-Halide Perovskite Solar Cells with n-Doped Organic Electron Extraction Layers. *Adv. Mater.* (2017) doi:10.1002/adma.201604186.

64. Solanki, A. *et al.* Cation influence on carrier dynamics in perovskite solar cells. *Nano Energy* **58**, 604–611 (2019).

65. Zhao, J. *et al. Strained hybrid perovskite thin films and their impact on the intrinsic stability of perovskite solar cells*. http://advances.sciencemag.org/ (2017).

66. Jones, W. *et al.* Lattice Strain Causes Non-Radiative Losses in Halide Perovskites. *Energy Environ. Sci* (2019) doi:10.1039/C8EE02751J.

67. van Roosbroeck, W. & Shockley, W. Photon-Radiative Recombination of Electrons and Holes in Germanium. *Phys. Rev.* **94**, 1953–1955 (1954).

68. Huang, J., Yuan, Y., Shao, Y. & Yan, Y. Understanding the physical properties of hybrid perovskites for photovoltaic applications. *Nature Reviews Materials* (2017) doi:10.1038/natrevmats.2017.42.

69. Kasap, S. O., Fogal, B., Kabir, M. Z., Johanson, R. E. & O'Leary, S. K. Recombination of drifting holes with trapped electrons in stabilized a-Se photoconductors: Langevin recombination. **1991**, 1–4 (2006).

70. Kandada, A. R. S. & Petrozza, A. Research Update : Luminescence in lead halide perovskites. *APL Mater.* **091506**, (2016).

71. Yang, W., Yao, Y. & Wu, C.-Q. Origin of the high open circuit voltage in planar heterojunction perovskite solar cells : Role of the reduced bimolecular recombination. *J. Appl. Phys.* **117**, (2015).

72. Lasher, G. & Stern, F. Spontaneous and Stimulated REcombination Radiation in Semidconductors. *Phys. Rev.* **133**, (1964).

73. Wehrenfennig, C., Liu, M., Snaith, H. J., Johnston, M. B. & Herz, L. M. Charge-carrier dynamics in vapour-deposited films of the organolead halide perovskite CH3NH3PbI3-xClx. *Energy Environ. Sci.* (2014) doi:10.1039/c4ee01358a.

74. Richter, J. M. *et al.* Enhancing photoluminescence yields in lead halide perovskites by photon recycling and light out-coupling. *Nat. Commun.* (2016) doi:10.1038/ncomms13941.

75. Manzoor, S. *et al.* Improved light management in planar silicon and perovskite solar cells using PDMS scattering layer. *Sol. Energy Mater. Sol. Cells* (2017) doi:10.1016/j.solmat.2017.06.020.

76. Schnitzer, I., Yablonovitch, E., Caneau, C. & Gmitter, T. J. Ultrahigh spontaneous emission quantum externally , from AlGaAs/GaAs/AlGaAs double heterostructures. *Appl. Phys. Lett.* **131**, (2013).

77. Braly, I. L. *et al.* Hybrid perovskite films approaching the radiative limit with over 90% photoluminescence quantum efficiency. *Nat. Photonics* (2018) doi:10.1038/s41566-018-0154-z.

78. Lin, Y. *et al.* π-Conjugated Lewis Base: Efficient Trap-Passivation and Charge-Extraction for Hybrid Perovskite Solar Cells. (2016) doi:10.1002/adma.201604545.

79. Fang, Y., Wei, H., Dong, Q. & Huang, J. Quantification of re-absorption and re-emission processes to determine photon recycling efficiency in perovskite single crystals. *Nat. Commun.* **8**, 1–9 (2017).

80. Beattie, A. R., Landsberg, P. T. & Froehlich, H. Auger effect in semiconductors. *Proc. R. Soc. A* (1959).

81. Trinh, M. T., Wu, X., Niesner, D. & Zhu, X. Many-body interactions in photo-excited lead iodide perovskite. *J. Mater. Chem. A* 9285–9290 (2015) doi:10.1039/c5ta01093d.

82. Dziewior, J. & Schmid, W. Auger coefficients for highly doped and highly excited silicon. *Appl. Phys. Lett.* **31**, 346–348 (1977).

83. Rehman, W. *et al.* Charge-Carrier Dynamics and Mobilities in Formamidinium Lead Mixed-Halide Perovskites. *Adv. Mater.* (2015) doi:10.1002/adma.201502969.

84. Haug, A. Auger recombination in direct-gap semiconductors : band-structure effects. *J. Phys. C Solid State Phys.* (1983).

85. Even, J., Pedesseau, L. & Katan, C. Analysis of multivalley and multibandgap absorption and enhancement of free carriers related to exciton screening in hybrid perovskites. *J. Phys. Chem. C* **118**, 11566–11572 (2014).

86. Shen, J. X., Zhang, X., Das, S., Kioupakis, E. & Van de Walle, C. G. Unexpectedly Strong Auger Recombination in Halide Perovskites. *Adv. Energy Mater.* (2018) doi:10.1002/aenm.201801027.

87. Xing, G. *et al.* Low-temperature solution-processed wavelength-tunable perovskites for lasing. *Nat. Mater.* **13**, 476–480 (2014).

88. Tiedje, T., Yablonovitch, E., Cody, G. D. & Brooks, B. G. Limiting Efficiency of Silicon Solar Cells. *IEEE Trans. Electron Devices* **31**, 711–716 (1984).

89. Sheik-Bahae, M. & Epstein, R. I. Can laser light cool semiconductors? *Phys. Rev. Lett.* **92**, 1–4 (2004).

90. Chen, B., Rudd, P. N., Yang, S., Yuan, Y. & Huang, J. Imperfections and their passivation in halide perovskite solar cells. *Chem. Soc. Rev.* **48**, 3842--3867 (2019).

91. Krogmeier, B., Staub, F., Grabowski, D., Rau, U. & Kirchartz, T. Quantitative analysis of the transient photoluminescence of CH 3 NH 3 PbI 3 /PC 61 BM heterojunctions by numerical simulations. *Sustain. Energy Fuels* **2**, 1027–1034 (2018).

92. Maiberg, M. & Scheer, R. Theoretical study of time-resolved luminescence in semiconductors. *IV. Lateral inhomogeneities J. Appl. Phys.* **116**, 22110 (2014).

93. Maiberg, M., Hölscher, T., Zahedi-Azad, S., Fränzel, W. & Scheer, R. Investigation of long lifetimes in Cu(In,Ga)Se2 by time-resolved photoluminescence. *Appl. Phys. Lett.* (2015) doi:10.1063/1.4931632.

94. Kanevce, A., Levi, D. H. & Kuciauskas, D. The role of drift, diffusion, and recombination in time-resolved photoluminescence of CdTe solar cells determined through numerical simulation. *Prog. Photovoltaics* 1138–1146 (2014) doi:10.1002/pip.

95. Zong, Y., Zhou, Z., Chen, M., Padture, N. P. & Zhou, Y. Lewis-Adduct Mediated Grain-Boundary Functionalization for Efficient Ideal-Bandgap Perovskite Solar Cells with Superior Stability. *Adv. Energy Mater.* **8**, 1–9 (2018).

96. Zheng, X. *et al.* Defect passivation in hybrid perovskite solar cells using quaternary ammonium halide anions and cations. *Nat. Energy* (2017) doi:10.1038/nenergy.2017.102.

97. Wu, B. *et al.* Discerning the Surface and Bulk Recombination Kinetics of Organic–Inorganic Halide Perovskite Single Crystals. *Adv. Energy Mater.* **6**, 1–9 (2016).

98. Shi, D. *et al.* Low Trap-State Density and Long Carrier Diffusion in Organolead Trihalide Perovskite Single Crystals. *Science (80-.).* **347**, 519–522 (2015).

99. Kim, J. *et al.* Excitation Density Dependent Photoluminescence Quenching and Charge Transfer Efficiencies in Hybrid Perovskite/Organic Semiconductor Bilayers. *Adv. Energy Mater.* **8**, 1–11 (2018).

100. Chirvony, V. S. *et al.* Delayed Luminescence in Lead Halide Perovskite Nanocrystals. *J. Phys. Chem. C* **121**, 13381–13390 (2017).

101. Yang, S. *et al.* Stabilizing halide perovskite surfaces for solar cell operation with wide-bandgap lead oxysalts. *Science (80-.).* **365**, 473–478 (2019).

102. Deng, Y. *et al.* Tailoring solvent coordination for high-speed, room-temperature blading of perovskite photovoltaic films. *Sci. Adv.* **5**, 1–9 (2019).

103. Wang, Q. *et al.* Scaling behavior of moisture-induced grain degradation in polycrystalline hybrid perovskite thin films. *Energy Environ. Sci.* (2016) doi:10.1039/c6ee02941h.

104. Zong, Y. W., Jian, B.-L. & Hsu, H.-C. Photoluminescence characterizations of highly ambient-air-stable CH3NH3PbI3/PbI2 heterostructure. *Opt. Mater. Express* **9**, 1882–1892 (2019).

105. Dobrovolsky, A. *et al.* Relating Defect Luminescence and Nonradiative Charge Recombination in MAPbI3 Perovskite Films. *J. Phys. Chem. Lett.* **11**, 1714–1720 (2020).

106. Smith, A. J., Wang, C., Guo, D., Sun, C. & Huang, J. Repurposing Blu-ray movie discs as quasi-random nanoimprinting templates for photon management. *Nat. Commun.* **5**, 1–5 (2014).